

Converging P-T paths of Mesozoic HP-LT metamorphic units (Diego de Almagro Island, Southern Chile): evidence for juxtaposition during late shortening of an active continental margin

A. P. Willner¹, F. Hervé², S. N. Thomson^{1,3}, and H.-J. Massonne⁴

¹ Institut für Geologie, Mineralogie und Geophysik, Ruhr-Universität, Bochum, Germany

² Departamento de Geología, Universidad de Chile, Santiago, Chile

³ Department of Geology and Geophysics, Yale University, New Haven, USA

⁴ Institut für Mineralogie und Kristallchemie, Technische Universität, Stuttgart, Germany

Received October 6, 2003; revised version accepted February 19, 2004

Editorial handling: J. G. Raith

Summary

On Diego de Almagro Island in Chilean Patagonia (51°30' S), a convergent strike slip zone, the Seno Arcabuz shear zone, separates the Diego de Almagro Metamorphic Complex from very low grade metagreywackes in the east, which were intruded by Jurassic granitoids. The Diego de Almagro Metamorphic Complex is composed of a metapsammopelitic sequence containing blueschist intercalations in the west and (garnet) amphibolite lenses in the east. Peak metamorphic conditions (stage I) at 9.5–13.5 kbar, 380–450 °C in the blueschist and at 11.2–13.2, 460–565 °C in the amphibolite indicate subduction and accretion at different positions within the deepest part of the accretionary wedge. A K–Ar age of 117 ± 28 Ma of amphibole approximately dates the peak of metamorphism in the amphibolite. The early retrograde stage of metamorphism occurred under static conditions and resulted in localized equilibration (stage II) at 6.3–9.6 kbar, 320–385 °C in the blueschist and 6.1–8.4 kbar, 310–504 °C in the amphibolite. Both P-T paths converge within a midcrustal level.

In contrast, an orthogneiss of trondhjemitic composition occurring within the Seno Arcabuz shear zone is associated with a garnet mica-schist containing a high temperature/intermediate pressure assemblage formed at 4.9–6.5 kbar, 580–690 °C.

A muscovite K–Ar age of 122.2 ± 4.6 Ma dates cooling after this event which is related to a concomitant magmatic arc. These rocks were overprinted by a mylonitic deformation, which is caused by convergent strike slip shearing and ends during formation of a retrograde phengite-chlorite-stilpnomelane assemblage at a minimum pressure of approximately 5.7 kbar (at 300 °C).

Zircon fission track ages from rocks of the Seno Arcabuz shear zone are 64.9 ± 2.7 and 64.9 ± 2.7 Ma; they record the end of shearing in the Seno Arcabuz shear zone that juxtaposed all rocks in the middle crust. Zircon fission track ages ranging from 78 to 105 Ma in the South Patagonian batholith to the east indicate earlier cooling through 280 °C. The rocks of the Diego de Almagro Metamorphic Complex were initially slowly exhumed and resided at a midcrustal level before being emplaced via shearing in the Seno Arcabuz shear zone. Apatite fission track ages (54 ± 8 Ma) from the Seno Arcabuz shear zone show that exhumation and cooling rates increased after this event. The incorporation of continental crust within the subduction system was a late process, which modified the Cretaceous accretionary wedge, resulting in considerable shortening of the convergent margin.

Introduction

Diego de Almagro Island (lat. $51^{\circ}30'$ S; Fig. 1) is a remote island in the southern Chilean archipelago W of the Cordillera Sarmiento. The first account of the geology of this island by *Cecioni* (1955) indicated the presence of Paleozoic rocks, but *Forsythe et al.* (1981) was the first to report blueschists in the southwestern portion of the island. However, no detailed information on these rocks was ever published. The second author had the opportunity to study these rocks again in 1997 and 1998 observing transitions to amphibolite facies rocks and an orthogneiss with a high pressure imprint. The latter seems to be a rare case of continental crust incorporated into a subduction setting at the South American convergent margin.

Diego de Almagro Island belongs to a semi-continuous belt of low grade metamorphic rocks, which constitute large parts of the present Chilean Coastal Cordillera between 26° S and 54° S (Fig. 1A) and originally continued into the South Shetland Islands of western Antarctica. This basement is considered to represent an extended system of fossil accretionary complexes developed at the southwestern margin of Gondwana during the Late Paleozoic and Mesozoic (*Hervé*, 1988), which are otherwise rare along the active continental margin of South America. The low grade metamorphic rock suite contains some very rare local occurrences of blueschist, but its overall high pressure-low temperature HP-LT nature is evidenced by abundant phengite within widespread metapsammopelitic rocks and intercalated metabasites, which are also rich in Na–Ca-amphibole (*Massonne et al.*, 1996; *Willner et al.*, 1999). The PT-evolution of several selected areas occurred under conditions of the overlapping fields of actinolite-pumpellyite, greenschist, epidote blueschist and albite amphibolite facies under metamorphic gradients between 10° and 15° C/km (*Willner et al.*, 2000, 2001, 2004). The ages of HP-LT metamorphism vary strongly along the chain of accretionary prisms: accretion processes occurred during Late Carboniferous to Mid-Triassic times in central Chile (*Hervé et al.*, 1982; *Martin et al.*, 1999) and during Mid-Triassic to Jurassic times in southern Chile (*Davidson et al.*, 1989; *Thomson and Hervé*, 2003).

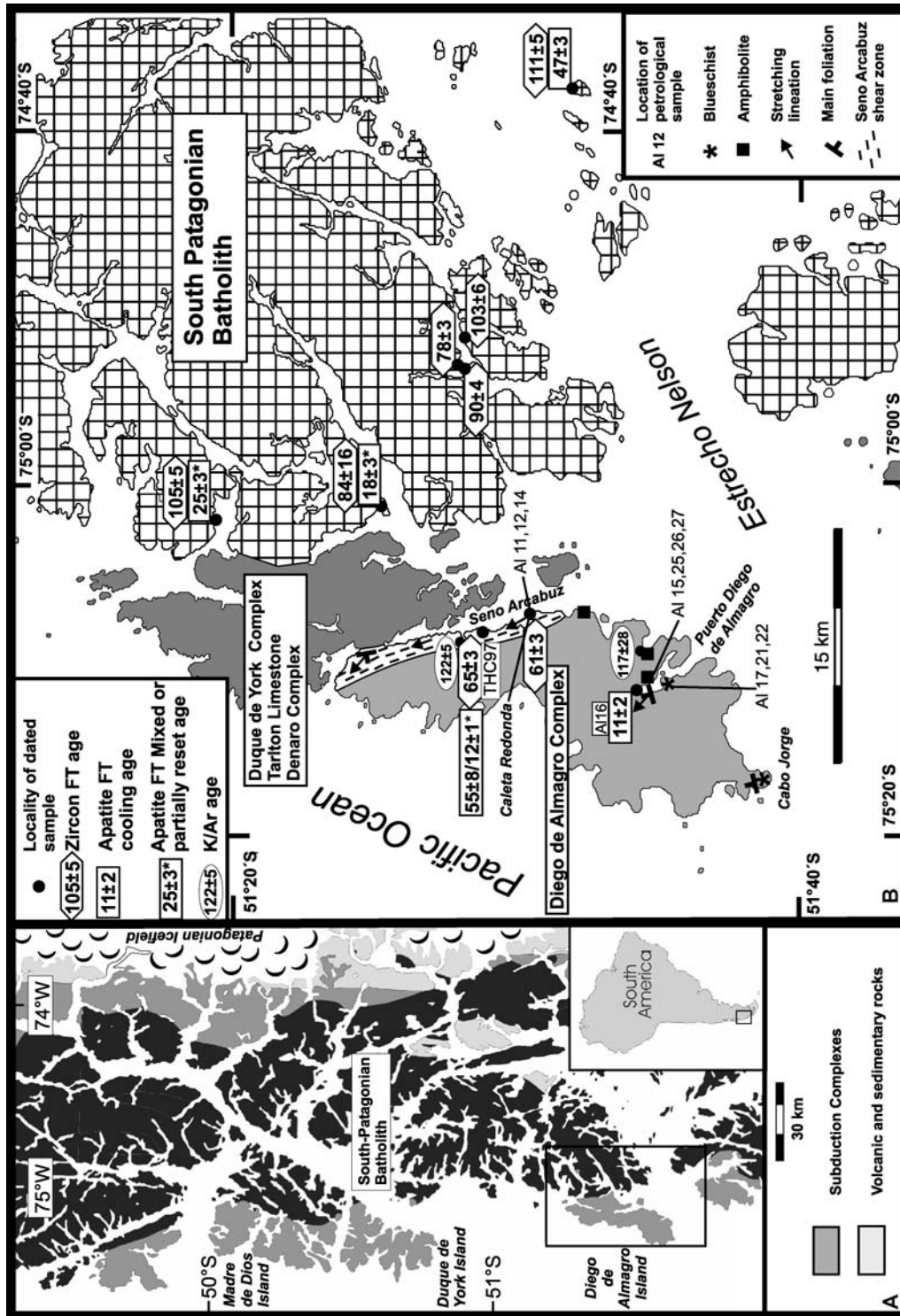


Fig. 1. Geological map of **a** Chilean southern Patagonia, **b** Diego de Almagro Island (including the ages derived in this study and the position of the petrological samples)

Our general aim was to study this rare situation, where HP-LT rocks revealing different geological evolutions are exposed over short distances. In particular, we wanted (1) to detect relationships between blueschist, amphibolite and nearby sedimentary rocks and continental crust incorporated into the subduction system, (2) to understand phase relationships at the boundary between epidote-blueschist facies and albite-epidote-amphibolite facies, (3) to establish partial PT-paths and provide time constraints for the evolution and exhumation history of this convergent margin, and (4) to compare these results with those from other related localities in southern Chile and the South Shetland Islands. The final goal is to gain a better understanding of the structure of HP belts and of processes related to the destruction of fossil accretionary systems.

Geological setting and field relationships

In the area studied (Fig. 1) three major complexes are distinguished: The Diego de Almagro Metamorphic Complex (DAMC) is composed of mica-schist, blueschist, amphibolite and ultramafic rocks and is separated toward the east from a block composed of the Tarlton limestone (TL), the Denaro (DC) and Duque de York (DYC) complexes by the Seno Arcabuz shear zone (SASZ).

The DAMC can be interpreted as a relic fossil accretionary prism. It was studied at Puerto Diego de Almagro bay (Fig. 1B), where (garnet) amphibolite and blueschist are intercalated in psammopelitic mica-schist on the centimetre to several hundreds of meters scale. *Forsythe et al.* (1981) also mentioned the presence of serpentinite, which was not sampled in this study. The two known blueschist localities are at Cabo Jorge and at the western shore of Puerto Diego de Almagro bay. The amphibolite is exposed at the eastern shore of the bay and along the coast further to the east (Fig. 1B). The blueschist is a fine-grained and well foliated rock type, with a pronounced alignment of amphibole and occasional occurrence of albite porphyroblasts. The amphibolite is slightly coarser grained, usually banded parallel to the main foliation and contains conspicuous albite porphyroblasts. The dominant subhorizontal foliation with NW-trending stretching lineations is folded on the meter to tens of meters scale into open to tight folds with roughly NS-trending fold axes. A thin layer of a greyish and fine-banded garnet-amphibole quartzite with conspicuous white mica occurs at the boundary between the blueschist and amphibolite areas at the northwestern end of the Puerto Diego de Almagro bay (Fig. 1B).

At the western shore of Seno Arcabuz a pronounced 2–3 km wide, NNW-trending ductile shear zone (SASZ) is exposed. The rocks within this shear zone document at least two ductile deformation events (*Olivares et al.*, 2003): an early mylonitic foliation and lineation, and a late low strain foliation and lineation originated by folding of the early fabric. Rock strain and metamorphic grade increase progressively toward the south. Kinematic indicators are mainly sinistral-reverse, although dextral-normal indicators were also observed (*Olivares et al.*, 2003).

At Caleta Redonda at the southern end of the SASZ a coarse-grained orthogneiss with a protomylonitic overprint is exposed (sample A112). The extension of this orthogneiss body is unknown. Light coloured veins, 5–10 cm thick, composed of a central quartz-rich band and coarse-grained quartz-albite-muscovite rims, are

isoclinally folded and may represent former pegmatitic veins. In addition amphibolite bands of similar size are found enclosed in the orthogneiss; presumably these were basic dykes. The contact between the orthogneiss and the DAMC to the west was not observed. Further north along the shear zone, garnet-bearing mica-schist predominates, with subordinate 0.1 to 0.4 m thick bands of (garnet) amphibolite showing a pervasive crenulation foliation and lineation. At the northernmost end of Seno Arcabuz, metasediments and slates prevail. They show the same structural inventory as the rocks further south.

The three complexes to the east of the SASZ were defined by *Forsythe and Mpodozis* (1983) on the Madre de Dios Island (Fig. 1A). The Tarlton limestone consists of massive pelagic limestone with Late Carboniferous to Early Permian fusulinides (*Douglas and Nestell, 1976*), which overlies and is in part coeval with a sequence of pillow basalts, metalliferous and radiolarian cherts and argillite, which comprise the oceanic Denaro Complex. The dominating Duque de York Complex is composed of very low grade and weakly deformed metagreywackes and shales with well preserved sedimentary structures and unconformably overlies the Tarlton limestone and the Denaro complex. These two complexes were interpreted by *Forsythe* (1982) as exotic blocks formed in an oceanic environment that were later transported and obducted onto the continental margin, where they were covered by the sediments of the Duque de York Complex. All eastern complexes were intruded by the Late Jurassic to Early Cretaceous calc-alkaline plutons of the South Patagonian Batholith at a very shallow crustal level. They remained at shallow crustal depth and constitute the frame to which the DAMC was finally juxtaposed; they are not considered in further detail in this study.

Analytical methods

Mineral analyses were obtained with a Cameca SX 50 microprobe at Ruhr-Universität Bochum, Germany. Operating conditions were an acceleration voltage of 15 kV, a beam current of 15 nA, 20s counting time per element and a defocused beam of 8 μm in order to avoid loss of alkalis in mica and amphibole. The following standards were used: synthetic pyrope [Si, Al, Mg], rutile [Ti], glass of andradite composition [Fe, Ca], jadeite [Na], K-bearing glass [K], NaCl [Cl], topaz [F], Cr_2O_3 [Cr], Ba-silicate glass [Ba ($L\alpha$)]. The PAP procedure was applied for matrix correction. Representative analyses and structural formulae of minerals used for PT-calculations are listed in the appendix together with the calculation procedure of the structural formulae. Abbreviations for minerals and mineral components used throughout the text follow *Kretz* (1983). Abbreviations not included in *Kretz* (1983) are: Kwm – K-white mica; Nam – Na-amphibole; Cam – Ca-amphibole; WM – white mica; V – vapour. All amphibole nomenclature is after *Leake et al.* (1997). Further analyses may be provided by the first author upon request.

For fission-track (FT) analysis, mounting, polishing and etching of zircon and apatite heavy mineral fractions were carried out at Ruhr-Universität Bochum using the methods outlined by *Hurford et al.* (1991). The samples were analysed applying the external detector method and irradiated with Corning dosimeter glasses (CN2 for zircon and CN5 for apatite) at the Oregon State University Triga Reactor,

Corvallis, USA. Central ages (*Galbraith and Laslett, 1993*), quoted with 1σ errors, were calculated using the IUGS approved zeta-calibration approach of *Hurford and Green (1983)*. Zeta calibration factors of 130.7 ± 2.8 for CN2 (zircon) and 358.8 ± 12.7 for CN5 (apatite) were obtained by repeated calibration against a number of internationally agreed age standards according to the recommendations of *Hurford (1990)*.

K–Ar analyses were performed in 1985 at the Centre of Geochronological Research of the University of Sao Paulo, Brazil following laboratory routine procedures and using an AEI MS10 mass spectrometer. Procedures were described in detail by *Amaral et al. (1966)*. The precision in the obtained ages is about 5%.

Petrography and mineral chemistry

We now describe rocks of the two entirely different metamorphic complexes, the DAMC and the SASZ, separately.

Diego de Almagro Metamorphic Complex

Amphibolite

The amphibolite samples (Al 15, 25, 26, 27) are strongly foliated rocks with the general assemblage: *Ca-amphibole – epidote – chlorite – albite – quartz – white mica – titanite ± garnet ± calcite ± ilmenite ± pyrite ± apatite*.

Strongly oriented and partly sheared crystals of *Ca-amphibole* are up to 2 mm long and makes up to 10–60% of the rocks. Amphibole shows a notable optical zoning with dark green cores and light bluish-green rims. Chemically the dark coloured cores of the amphibole (generation I) are classified as tschermakitic hornblende to magnesio-hornblende ($Si = 6.2–6.8$ p.f.u.; $X_{Mg} = Mg/(Mg + Fe) = 0.47–0.81$; $X_{Fe^{3+}} = Fe^{3+}/(Fe^{3+} + Al) = 0.16–0.58$; Fig. 2) with a notable content of Na^A (0.23–0.76 p.f.u.; compositions of some grains extend into the fields of pargasitic hornblende to edenite) and of Na^B (0.15–0.65 p.f.u). The rims (generation II) are actinolitic hornblende to actinolite ($Si = 6.95–7.86$ p.f.u.; $X_{Mg} = 0.48–0.65$) with less Na^B (0.06–0.36 p.f.u.) and higher $X_{Fe^{3+}}$ (0.37–0.42) than the first generation. In one sample (Al 25) compositions extend into the field of winchite/barroisite ($Na^B = 0.7–0.8$ p.f.u.; $Si = 7.2–7.8$ p.f.u.). Amphibole inclusions in garnet of sample Al 27 correspond to generation I.

Chlorite, epidote and titanite are either interstitial to the amphibole crystals or form monomineralic aggregates and lenses. *Chlorite* shows little intrasample variation ($X_{Mg} = 0.6–0.39$; $Si = 5.35–5.85$ p.f.u.) and generally no clear zoning, although X_{Mg} may tend to increase towards the rims. Chlorite inclusions in garnet and amphibole in sample Al 27 have a distinctly higher X_{Mg} (0.57–0.59) compared to matrix chlorite (0.39–0.47). Chlorite also replaces garnet and amphibole. Fe^{3+} contents in *epidote* vary between 0.46 and 0.86 p.f.u. and increase towards the rims. *Titanite* forms strings and pods parallel to the foliation. It yields a low abundance of Al and Fe^{3+} (0.05–0.10 p.f.u.) and is of rather homogeneous composition. Albite either forms interstitial crystals or occurs as up to 1 mm large porphyroblasts; the latter partly contain S-shaped inclusion trails indicating synkinematic

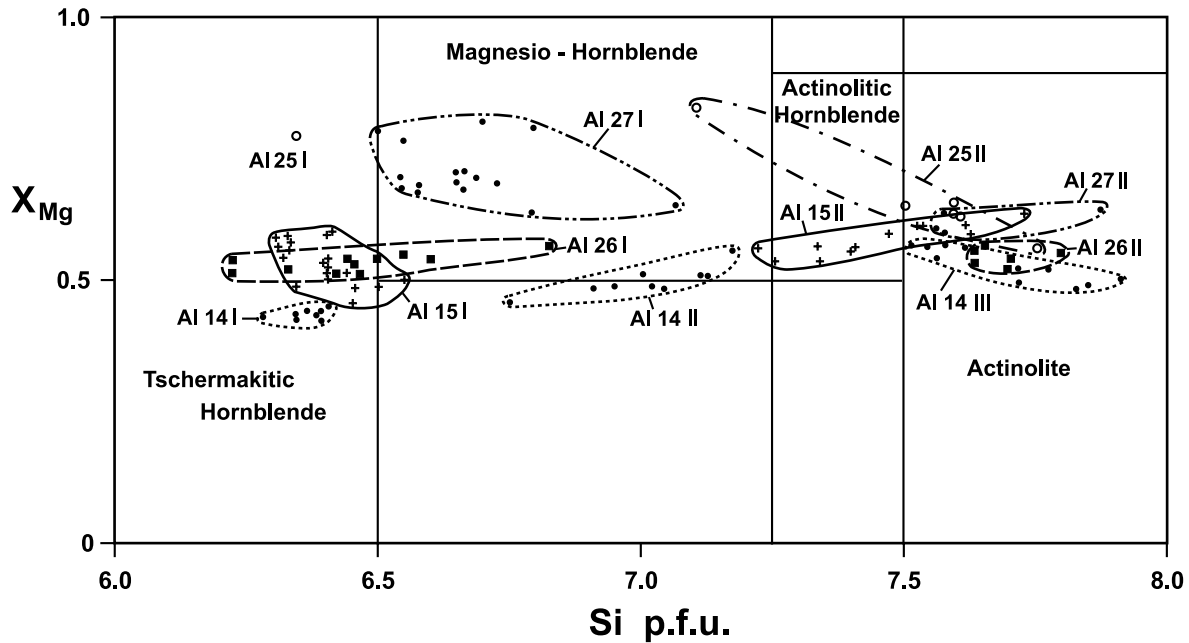


Fig. 2. X_{Mg} -Si variation of Ca-amphibole in amphibolite samples

growth of albite. Quartz is present in ribbons and commonly shows undulose extinction.

White mica forms scattered flakes and is phengite with Si-contents in the range of 3.32–3.46 Si p.f.u. and a trend of decreasing Si-contents toward the rims. Sample Al 27 contains abundant subhedral *garnet* (~30%) with inclusions of albite, quartz, chlorite, ilmenite, titanite and Ca-amphibole. Garnet is partially altered to chlorite and shows little compositional variation (almandine_{0.53–0.61}, pyrope_{0.20–0.22}, grossular_{0.20–0.22}, spessartine_{0.01–0.02}).

Blueschist

The blueschist (samples Al 17, 21, 22) is a well foliated rock type with the assemblage *blue amphibole – epidote – albite – quartz – white mica – chlorite – titanite ± calcite ± magnetite ± apatite*.

The main foliation is defined by alternating bands enriched in amphibole or chlorite-epidote-titanite or white mica or quartz and by the alignment of amphibole. It is crenulated by a second foliation. *Amphibole* is strongly zoned showing blue cores and green rims. Similar to the amphibolite, two generations can be distinguished. Generation I is represented by glaucophane ($Na^B = 1.5–1.97$ p.f.u., $X_{Mg} = 0.48–0.72$ p.f.u., $X_{Fe^{3+}} = 0.13–0.53$; Fig. 3) and generation II consists of Na-rich actinolite ranging into the field of Fe-rich winchite or barroisite ($Na^B = 0.24–1.3$ p.f.u., $(Na + K)^A = 0.1–0.54$ p.f.u., $X_{Mg} = 0.46–0.72$, $X_{Fe^{3+}} = 0.11–0.84$; Si = 6.98–7.80 p.f.u.; Fig. 3a). The Fe^{3+} -contents of *epidote* vary in the range 0.77–0.94 p.f.u. increasing or decreasing towards the rims. *Titanite* forms

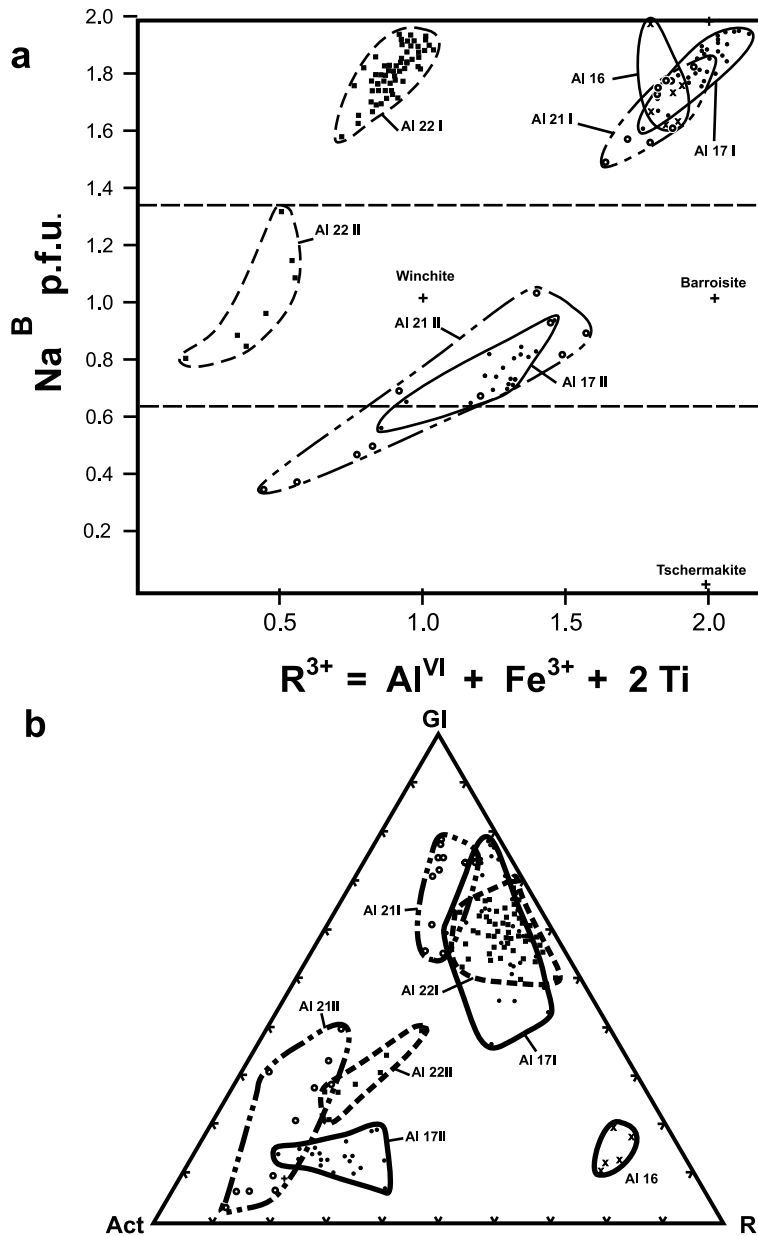


Fig. 3. Variation of amphibole compositions in blueschist samples **a** Na^B versus R^{3+} **b** system of endmember components glaucophane-actinolite-riebeckite: $X_{glau} = (2-Ca) / 2 * Al^{VI} / (Al^{VI} + Fe^{3+})$; $X_{act} = Ca / 2$; $X_{rieb} = 1 - (X_{glau} + X_{act})$

Pods or strings and has low $Al + Fe^{3+}$ contents (0.04–0.08 p.f.u.). *Albite* forms porphyroblasts with inclusion trails of different orientation within the grains. *Chlorite* is interstitial and shows little compositional variation ($X_{Mg} = 0.44–0.52$; $Si = 5.4–5.65$ p.f.u.). Strongly oriented *white mica* is phengitic (3.2–3.5 Si p.f.u.; Fig. 4). Si-contents can increase or decrease towards the rims. The Ca–Mn-rich

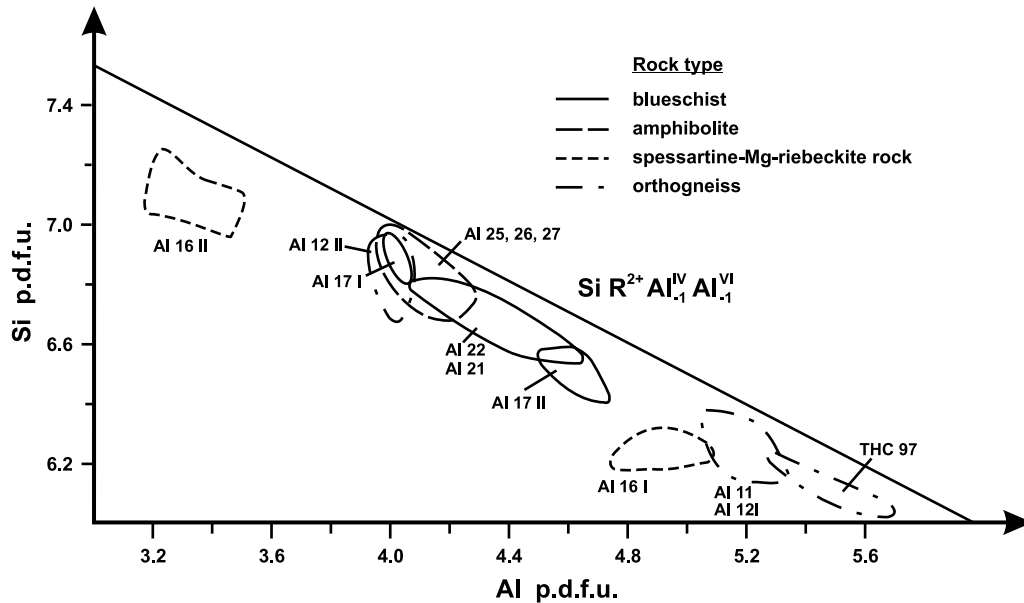


Fig. 4. Plot showing Si versus Al for white mica compositions. The line of the ideal Tschermak substitution is indicated

sample Al 21 contains bands with occasional small garnet grains (around 50 μm). Garnet shows little compositional variation (almandine_{0.43–0.55}, grossular_{0.30–0.33}, spessartine_{0.10–0.22}, pyrope_{0.03–0.04}).

Spessartine-Mg-riebeckite quartzite

Sample Al 16 is a conspicuous greyish, finely banded and quartz-rich protomylonite from the western end of Puerto Diego de Almagro occurring between the blueschist and the amphibolite areas. Its primary metamorphic assemblage is *quartz – albite – white mica – biotite – blue amphibole – garnet – magnetite ± tourmaline*. Predominant *quartz* forms bands of strongly elongated original grains with abundant subgrain boundaries, sutured grain boundaries and beginning subgrain formation. Occasional *albite* shows larger crystal size, white mica inclusions and brittle deformation. Blue amphibole, white mica, biotite and stilpnomelane form aggregates of variable size with unoriented grains. *White mica* displays light green colour and notable pleochroism and exists in two different generations: big crystals with Si contents of 3.07–3.13 p.f.u. (WM I) and smaller crystals, some peripheral to biotite grains, and rims of larger crystals with Si-contents of 3.45–3.61 p.f.u. (WM II) respectively (Fig. 4). Both generations have distinctly different contents of Ba (WM I: 0.035–0.05 p.f.u.; WM II < 0.03 p.f.u.), Ti (WM I: 0.01–0.08 p.f.u.; WM II < 0.01 p.f.u.), Mn (WM I: < 0.01 p.f.u.; WM II: 0.015–0.04 p.f.u.) and Na (WM I 0.035–0.05 p.f.u.; WM II 0.005–0.01 p.f.u.). Both generations have high Fe-contents ($X_{\text{Fe}} = 0.48–0.70$; Fe^{3+} 0.12–0.39 p.f.u.). Greenish brown *biotite* is enriched in Fe ($X_{\text{Fe}} = 5.4–6.1$), Mn (0.05–0.07 p.f.u.) and Ba (0.02–0.04 p.f.u.). Two generations of biotite are present: a possible high

temperature generation ($X_{\text{Mg}} = 0.38\text{--}0.46$; $\text{Ti} = 0.26\text{--}0.33$ p.f.u.) and a second generation ($X_{\text{Mg}} = 0.50\text{--}0.52$; $\text{Ti} = 0.05\text{--}0.11$ p.f.u.). Biotite is replaced by *stilpnomelane* ($\text{Mn} 0.45\text{--}0.84$ p.f.u., $\text{Ba} 0.05\text{--}0.49$ p.f.u.) and the generation II of white mica.

Spessartine-rich *garnet* occurs as scattered small subhedral crystals with compositional variation of spessartine_{0.35–0.55}, almandine_{0.30–0.44}, pyrope_{0.05–0.12} and grossular_{0.08–0.10}. Zoning is weakly developed with slightly increasing Mn and Ca and decreasing Fe and Mg toward the rims. The *blue amphibole* is Mg-riebeckite ($\text{Na}^{\text{B}} = 1.6\text{--}1.8$ p.f.u., $X_{\text{Fe}^{3+}} = 0.79\text{--}0.89$, $X_{\text{Mg}} = 0.53\text{--}0.62$) without Ca-amphibole rims (Fig. 3).

The magmatic zircons obtained from this sample have a rather uniform age, which suggests that the rock may have originated as a tuff (*Herve and Fanning, 2003*). On the other hand, the spessartine-Mg-riebeckite quartzite shows strong enrichment of Mn, Ba and Fe with respect to a normal igneous rock and resembles cotecules (spessartine quartzite) which are frequently observed in the metamorphic basement of Central Chile (e.g. *Bahia Mansa, Willner et al., 2001*). These authors interpret the unusual chemical composition of such rocks as due to a pre-metamorphic hydrothermal overprint of the protolith.

Seno Arcabuz shear zone

Orthogneiss

The orthogneiss of Caleta Redonda (samples Al 11 and Al 12) shows two superimposed mineral assemblages and associated fabrics. The original assemblage of the gneissose protolith was *quartz – plagioclase – muscovite – biotite – apatite* pointing to a trondhjemitic composition. Feldspar and mica crystals are coarse-grained and have similar grain size (0.5–4 mm). Both micas are intergrown parallel (001) and reveal a mimetic orientation parallel to an original gneissose foliation. Small quartz veins developed parallel to this relic foliation. *Plagioclase* (~30%) occurs as porphyroclasts and is completely transformed to either epidote and albite or more frequently to a very fine-grained kelyphitic aggregate, which appears almost opaque in thin sections. Qualitative analyses show that the aggregate consists of epidote-albite intergrowths. Ghost-like albite twinning is always detectable in these pseudomorphs. The porphyroclasts are partly oriented parallel to the stretching lineation. The large *white mica* (~20%) is muscovite ($\text{Si} = 3.03\text{--}3.15$ p.f.u.; $\text{Na} = 0.04\text{--}0.05$ p.f.u.; $X_{\text{Mg}} = 0.50\text{--}0.56$; $\text{Ti} = 0.04\text{--}0.11$ p.f.u.), while the reddish brown *biotite* crystals (~10%) are also relatively Ti-rich (0.15–0.17 p.f.u.) with $X_{\text{Mg}} = 0.35\text{--}0.39$. Both micas are partly kinked or form mica fishes. *Quartz* (0.05–2.5 mm; 30%) generally exhibits strong undulose extinction and deformation bands with subgrain formation within elongated sigmoidal aggregates. *Apatite* of up to 2 mm size, *zircon* and *ilmenite* are accessory minerals.

The original gneissose fabric is overprinted by a protomylonitic foliation with quartz showing ductile deformation and feldspar showing brittle deformation. A second low temperature assemblage crystallized during and after this second deformation: *quartz – phengite – stilpnomelane – chlorite – epidote – albite*. The second

generation of white mica, being of smaller size (0.05–0.1 mm) than the first one, is *phengite* of variable composition (Si = 3.32–3.46 p.f.u.; Na = 0.015–0.2 p.f.u.; X_{Mg} = 0.55–0.80; Ti = 0.001–0.012 p.f.u.; Fig. 4). It grew in anastomosed C domains together with quartz or at the rims of the large muscovite crystals. *Stilpnomelane* aggregates occasionally grew in pressure shadows. *Chlorite* formed from biotite, whereas *epidote* and *albite* formed by alteration of plagioclase.

Amphibolite

The amphibolite (sample Al 14), which is associated with the orthogneiss at Caleta Redonda contains a strongly oriented coarse-grained (0.5–3 mm) assemblage with *hornblende – quartz – plagioclase – epidote – titanite*. The *amphibole* (~60%) is tschermakitic hornblende or magnesiohornblende in the core with actinolitic overgrowths at the rim (Fig. 2). Notably the amphibole does not contain any Na in the M4-position, but both generations differ considerably by the contents of the A position (hornblende 0.53–0.69 p.f.u., actinolite 0.16–0.39 p.f.u.) and X_{Mg} (hornblende 0.42–0.46, actinolite 0.49–0.57). Pseudomorphs after *plagioclase* (~10%) consisting of fine-grained kelyphitic intergrowths and albite, similar to those observed in the orthogneiss, occur between the oriented amphibole as does *titanite* (~5%) and *epidote* (~15%). The latter contains 40–46 mole % of pistacite component. *Quartz* (~10%) forms tiny pods or lenses parallel to the main foliation. The rock is overprinted by discrete shear bands with occasionally newly grown phengite (Si = 3.45 p.f.u.) and chlorite.

Garnet mica-schist

Sample THC97 is a garnet mica-schist overprinted by a retrograde deformation giving rise to a S-C fabric with discrete shear bands and quartz aggregates. These show orientation of formerly coarse quartz grains by lattice gliding and recrystallization of small neoblasts. Plagioclase has undergone brittle deformation.

The original fabric is defined by oriented intergrowths of white mica and biotite (0.5–2 mm) that grew mimetically after a second foliation, which still contains some crenulation relics. The white mica is muscovite (Si = 3.04–3.12 p.f.u.; Ti = 0.01–0.06 p.f.u.; Na = 0.1–0.2 p.f.u.; X_{Mg} = 0.52–0.54), while the reddish brown biotite is of intermediate composition (X_{Mg} = 0.44–0.52; Ti = 0.07–0.14 p.f.u.). Hypidioblastic garnet contains helicitic trails of graphite, biotite and white mica inclusions. Unoriented quartz inclusions near the garnet rims represent an original coarse-grained polygonal fabric. Garnet composition is almandine_{0.73–0.79}, pyrope_{0.11–0.20}, grossular_{0.043–0.051}, spessartine_{0.094–0.053} and andradite_{0.006–0.014}. Garnet zonation is characterized by relatively unzoned cores and an inverse zonation toward the rims with increasing Mn and Fe and decreasing Mg, whereas Ca does not reveal a clear trend. Large oriented tourmaline grains grew parallel to the main foliation and host helicitic graphite inclusion trails. Plagioclase is of intermediate composition (An₂₃), often forming large porphyroblasts that overgrew garnet, micas and quartz. Apart from recrystallised quartz, only a few newly grown grains of sericitic white mica were observed. This second white mica generation is phengitic (Si = 3.22 p.f.u.; X_{Mg} = 0.61; Na = 0.08 p.f.u.).

Phase relationships and geothermobarometry

From the above petrographic relationships it is concluded that the relative timing of growth especially of phengite is entirely different in the following two sets of rocks: (1) the high pressure rocks of the DAMC, with a growth of phengite at peak metamorphic conditions and (2) rocks of the SASZ, with a retrograde growth of phengite. Due to similarities in their metamorphic evolution we will consider the spessartine-Mg-riebeckite quartzite (Al 16) together with the latter.

Metabasites of the Diego de Almagro Metamorphic Complex

Two adjacent areas were detected in the DAMC with metabasites characterized by assemblages of the epidote-blueschist facies and of the albite-epidote-amphibolite facies. In order to assess the PT-stability fields for these assemblages we calculated pseudosections from representative whole rock bulk compositions of these two sets of rocks (samples Al 17 and Al 26) in the system $K_2O-Na_2O-CaO-TiO_2-Fe_2O_3-FeO-MgO-Al_2O_3-SiO_2-H_2O$ (Fig. 5). The Gibbs free energy minimization procedure was applied with the DEKAP code developed by Gerya et al. (2001). The calculation of the petrogenetic grid was performed with a resolution of 5 K and 100 bar for T and P, respectively. Thermodynamic data for minerals and aqueous fluid were taken from Holland and Powell (1998a). References to the mixing models applied, which are consistent with this database, are listed in Table 1. Figure 5 shows the stability fields of high-variance mineral assemblages at defined P-T conditions for the selected blueschist and amphibolite compositions. The peak metamorphic assemblage (stage I) of the blueschist occupies a field A at $P > 9$ kbar and $T < 440^\circ C$ with Na-amphibole (calculated glaucophane) as the only amphibole present together with chlorite, phengite and epidote, whereas the stage I assemblage of the amphibolite occupies a field C at $P > 7$ kbar and $T > 450^\circ C$ with Ca-amphibole (calculated Na-rich hornblende) as the only amphibole present together with phengite, albite and epidote above the stability field of biotite. Both assemblages occupy P-T stability fields at similar pressure ranges, but significantly different temperature ranges. Both fields are separated by calculated stability fields with two coexisting amphiboles similar to the transition between blueschist and greenschist assemblages. The two coexisting amphiboles would predict a miscibility gap. However, rocks, which were metamorphosed to the P-T range of these transitional fields, appear not to be exposed in the study area. In both calculated assemblages rutile would be a stable phase coexisting with titanite, but it was not observed in the samples. Nevertheless, it might have disappeared during retrograde reactions. On the other hand the retrograde mineral assemblages (stage II) of both rock types occupy similar stability fields (B and D at $P < 8$ kbar and $T < 450^\circ C$) with a Ca-amphibole (calculated Na-rich actinolite) present together with phengite, albite, chlorite and epidote and still above the stability field of biotite. Fields B and D thus represent the high pressure and high temperature part of the greenschist facies field. Retrograde rims developed during continuous reactions rather point to a continuous compositional transition of the amphiboles of both contrasting peak assemblages to typical greenschist facies amphiboles without the existence of miscibility gaps.

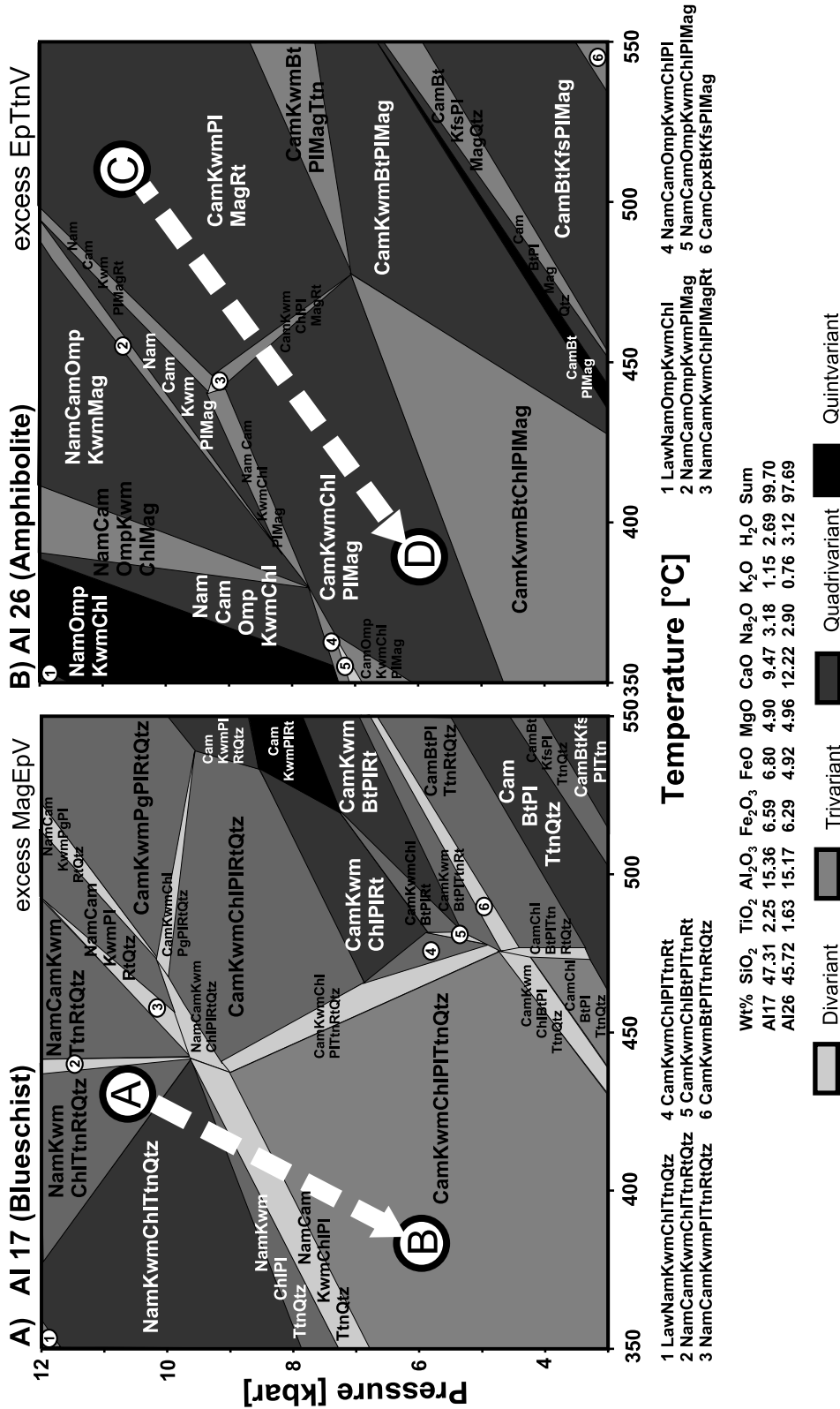


Fig. 5. Pseudosections calculated in the system SiO₂-TiO₂-Al₂O₃-Fe₂O₃-FeO-MgO-CaO-Na₂O-K₂O-H₂O for representative whole rock compositions of **a** blueschist (sample Al 17), **b** amphibolite (sample Al 26). For thermodynamic data and activity models see Table 1. Possible P-T paths are given by the sequence of assemblages A to B resp. C to D. Abbreviations not following *Kretz* (1983) are: *Kwm* K-white mica; *Nam* Na-amphibole; *Cam* Ca-amphibole; *V* vapour. Analyses were done at Universidad Nacional de Chile Santiago by XRF except Fe²⁺ and H₂O (standard wet chemical methods)

Table 1. References for thermodynamic data and activity models used for the different thermobarometric approaches

Mineral	Components	End member data	Activity formulation
<i>For calculation of the pseudosections</i>			
Clinopyroxene	jadeite, diopside, hedenbergite omphacite	Holland and Powell (1998a)	Vinograd (2002a, b)
Na-amphibole	glaucophane, tremolite, tschermakite Fe-glaucophane	Holland and Powell (1998a)	Will et al. (1998)
Ca-amphibole	glaucophane, tremolite, tschermakite Fe-actinolite, pargasite	Holland and Powell (1998a)	Dale et al. (2000)
Paragonite	paragonite, margarite	Holland and Powell (1998a)	Will et al. (1998)
K-white mica	muscovite, Mg-Al-celadonite, Fe-Al-celadonite, paragonite	Holland and Powell (1998a)	Powell et al. (1999)
Biotite	annite, phlogopite, eastonite, ordered biotite	Holland and Powell (1998a)	Powell et al. (1999)
Chlorite	clinochlore, daphnite, Mg-amesite Al-free chlorite	Holland and Powell (1998a)	Holland and Powell (1998b)
Plagioclase	anorthite, albite	Holland and Powell (1998a)	Will et al. (1998)
Epidote	clinozoisite, epidote, Fe-epidote	Holland and Powell (1998a) Holland and Powell (1998a)	Will et al. (1998)
Rutile, titanite, quartz Magnetite, Lawsonite, K-Feldspar		Holland and Powell (1998a) a = 1	
<i>For calculation of the multivariant reactions</i>			
Amphibole	glaucophane tremolite	Evans (1990) Berman (1988)	Massonne (1995a, b) Massonne (1995a, b)
Chlorite	clinochlore daphnite	Massonne (1995b) Massonne and Szpurka (1997)	Massonne (1995a) as Massonne (1995a)
Epidote	clinozoisite	Berman (1988)	as Massonne (1995a) $a_{\text{Clinozoisite}} = 1 - X_{\text{Pistazite}}$

(continued)

Table 1 (continued)

Garnet	grossular pyrope almandine muscovite	<i>Berman</i> (1990) <i>Berman</i> (1990) <i>Berman</i> (1990) <i>Massonne and Szpurka</i> (1997) <i>Massonne</i> (1997)	<i>Berman</i> (1990) <i>Berman</i> (1990) <i>Berman</i> (1990) <i>Massonne</i> (1997)
K-white mica	Mg-Al-celadonite Fe-Al-celadonite	<i>Massonne</i> (1995b) <i>Massonne</i> (1995b)	<i>Massonne</i> (1995b, 1997) <i>Massonne</i> (1995b, 1997)
Biotite	phlogopite Annite albite	<i>Berman</i> (1988) <i>Berman</i> (1990) <i>Berman</i> (1988) <i>Berman</i> (1988) <i>Berman</i> (1988)	<i>McMullin</i> et al. (1991) <i>McMullin</i> et al. (1991) $X_{\text{albite}} = X_{\text{albite}}$
Plagioclase Quartz K-feldspar			

Table 2. List of calculated multivariant reactions

(E1)	$6 \text{ clinozoisite}_{\text{ep}} + 7 \text{ quartz} + 11 \text{ glaucophane}_{\text{amp}} + 10 \text{ Fe-Al-celadonite}_{\text{wm}}$ $= 22 \text{ albite} + 3 \text{ Mg-Al-celadonite}_{\text{wm}} + 2 \text{ daphnite}_{\text{chl}} + 7 \text{ muscovite}_{\text{wm}} + 6 \text{ tremolite}_{\text{amp}}$
(E2)	$6 \text{ clinozoisite}_{\text{ep}} + 7 \text{ quartz} + 11 \text{ glaucophane}_{\text{amp}} + 7 \text{ Mg-Al-celadonite}_{\text{wm}}$ $= 22 \text{ albite} + 2 \text{ clinocllore}_{\text{chl}} + 7 \text{ muscovite}_{\text{wm}} + 6 \text{ tremolite}_{\text{amp}}$
(E3)	$\text{daphnite}_{\text{chl}} + 5 \text{ Mg-Al-celadonite}_{\text{wm}} = 5 \text{ Fe-Al-celadonite}_{\text{wm}} + \text{clinocllore}_{\text{chl}}$
(E4)	$30 \text{ clinozoisite}_{\text{ep}} + 35 \text{ quartz} + 55 \text{ glaucophane}_{\text{amp}} + 35 \text{ Fe-Al-celadonite}_{\text{wm}}$ $= 110 \text{ albite} + 7 \text{ daphnite}_{\text{chl}} + 3 \text{ clinocllore}_{\text{chl}} + 35 \text{ muscovite}_{\text{wm}} + 30 \text{ tremolite}_{\text{amp}}$
(E5)	$\text{almandine}_{\text{grt}} + 3 \text{ Mg-Al-celadonite}_{\text{wm}} = 6 \text{ quartz} + \text{phlogopite}_{\text{bt}} + \text{muscovite}_{\text{wm}} + \text{annite}_{\text{bt}}$
(E6)	$\text{almandine}_{\text{grt}} + 3 \text{ Mg-Al-celadonite}_{\text{wm}} = 6 \text{ quartz} + \text{pyrope}_{\text{grt}} + \text{muscovite}_{\text{wm}} + 2 \text{ annite}_{\text{bt}}$
(E7)	$\text{almandine}_{\text{grt}} + \text{phlogopite}_{\text{bt}} = \text{pyrope}_{\text{grt}} + \text{annite}_{\text{bt}}$
(E8)	$\text{pyrope}_{\text{grt}} + 3 \text{ Mg-Al-celadonite}_{\text{wm}} = \text{muscovite}_{\text{wm}} + 2 \text{ phlogopite}_{\text{bt}} + 6 \text{ quartz}$
(E9)	$3 \text{ Mg-Al-celadonite}_{\text{wm}} = 3 \text{ quartz} + 2 \text{ K-feldspar} + \text{phlogopite}_{\text{bt}} + 2 \text{ H}_2\text{O}$
(E10)	$5 \text{ Mg-Al-celadonite}_{\text{wm}} + \text{muscovite}_{\text{wm}} = 2 \text{ quartz} + 6 \text{ K-feldspar} + \text{clinocllore}_{\text{chl}} + 2 \text{ H}_2\text{O}$
(E11)	$2 \text{ glaucophane}_{\text{amp}} + 3 \text{ Mg-Al-celadonite}_{\text{wm}} = 4 \text{ albite} + 3 \text{ phlogopite}_{\text{bt}} + 7 \text{ quartz} + 2 \text{ H}_2\text{O}$
(E12)	$3 \text{ Mg-Al-celadonite}_{\text{wm}} + 2 \text{ albite} = \text{glaucophane}_{\text{am}} + 3 \text{ K-feldspar} + \text{quartz} + \text{H}_2\text{O}$

In order to test equilibrium conditions and to quantify P-T conditions for equilibration stages along the P-T path, we calculated local equilibria with multivariant reactions using mineral compositions of phases in close contact. Multivariant equilibria calculations were undertaken mainly using the Geocalc-software of *Brown et al. (1989)* and derivations (TWQ) with the thermodynamic data set of *Berman (1988)* with compatible additional data and activity models as summarized in Table 1. A list of the calculated reactions is given in Table 2. Results are summarized in Fig. 6 and listed in Table 3.

The two generations of amphibole in the two different metabasite rock types reflect two stages of equilibration along a partial P-T path, a peak metamorphic stage I and a retrograde stage II. For both stages calculations were performed utilizing coexisting minerals in close contact containing the relatively highest and lowest respective components to comprise the entire P-T ranges for both equilibration stages.

Calculations of invariant points for equilibria E1–4 using mineral core compositions result in a scatter of P-T data in the range of 9.5–13.5 kbar, 380–450 °C reflecting the stage I conditions in the blueschist and at 11.2–13.2 kbar, 460–565 °C for the amphibolite (Fig. 6; Table 3). The scatter presumably represents continuous equilibration in local domains around peak P-T conditions during the late prograde and early retrograde P-T path that could not be resolved in detail in the present case. For two samples conventional Fe–Mg exchange thermometry with garnet–amphibole pairs (*Graham and Powell, 1984*) was applied for comparison. Calculated temperatures range between 407 and 451 °C for the blueschist and between 459 and 517 °C for the amphibolite. Core compositions of mineral pairs yielded lower temperatures, rim compositions higher temperatures (Table 3). Evidently garnet grew during the late prograde P-T path in both metabasites.

Calculations of the stage II conditions with the same set of multivariant reactions but using rim compositions of phases in mutual contact yielded a scatter of P-T data in the range of 6.3–9.6 kbar, 320–385 °C for the blueschist

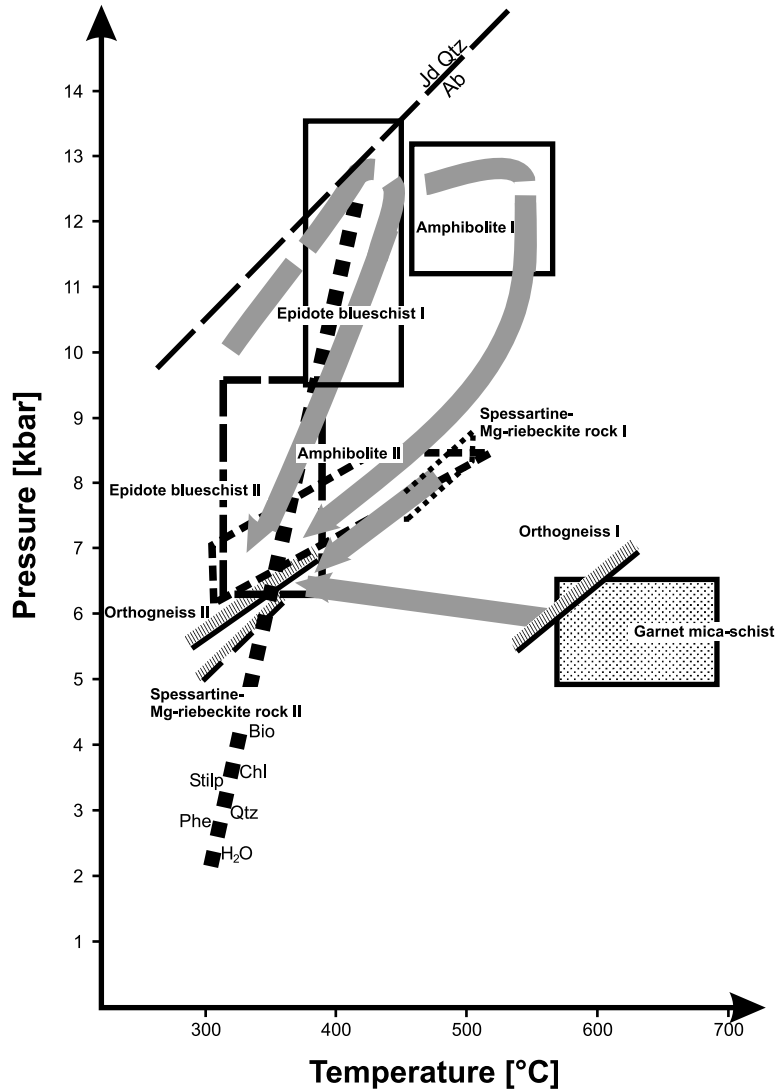


Fig. 6. Converging P-T paths of the rock units studied derived by calculating multivariant reactions. The albite breakdown reaction is taken from *Holland (1980)*, the stilp + phe – breakdown reaction is from *Massonne and Szpurka (1997)*. Boxes comprising calculated PT-values of two equilibration stages (I and II) are given for each rock type. Hatched curves for the orthogneiss and the spessartine-Mg-riebeckite rock indicate calculated minimum pressures (reactions E9, E10, E12 in Table 2)

and 6.1–8.4 kbar, 310–505 °C for the amphibolite. Thus equilibration during continuous mineral growth and recrystallization in localized domains resulted during continuous reaction proceeding during pressure release. Both ranges overlap at the lower P-T conditions. Clockwise P-T paths result for both the blueschist and the amphibolite. However, retrograde cooling during early decompression was more pronounced in the amphibolite than in the blueschist.

Table 3. Calculated pressures and temperatures

Sample	Coexisting assemblage	P [kbar]	T [°C]	Calculated equilibria (s. Table 3)	Comment	Sample	Coexisting assemblage	P [kbar]	T [°C]	Calculated equilibria (s. Table 3)	Comment	
Blueschist												
<i>Stage I</i>												
A117	A	13.5	410	E1-4		TCH97	A	4.9	578	E5-8	rim-rim	
B	12.7	428	E1-4		B		6.5	653	E5-8	rim-rim		
C	12.1	416	E1-4		C		6.0	690	E5-8	rim-rim		
A121	A	12.5	407	E1-4		Orthogneiss <i>Stage I</i> A112	D	5.6	665	E5-8	rim-rim	
B	9.5	379	E1-4		A		6.1	(575)	E9			
C	451	*		rim-rim								
D	447	*		rim-rim	<i>Stage II</i>							
E	436	*		core-core			B	5.7	(300)	E10		
F	407	*		core-core								
Spessartine-Mg-riebeckite rock												
A122	A	9.5	385	E1-4		<i>Stage I</i>						
<i>Stage II</i>												
A117	D	9.4	384	E1-4		A			464	*		
E	6.3	350	E1-4		B				497	*		
A121	G	7.6	353	E1-4		C			505	*		
	H	9.6	374	E1-4		D	7.6	(460)	(460)	E11		
A122	B	7.4	320	E1-4		E	8.6	(460)	(460)	E11		
Amphibolite												
<i>Stage I</i>												
A125	A	12.8	508	E1-4		F	5.6	(340)	(340)	E12		
B	11.9	530	E1-4									

(continued)

Table 3 (continued)

Al26	A	11.7	511	E1-4	
	B	11.2	503	E1-4	
Al27	A	13.2	563	E1-4	
	B	13.0	565	E1-4	
	C		517	*	rim-rim
	D		470	*	core-core
	E		459	*	core-core
<i>Stage II</i>					
Al25	C	6.5	384	E1-4	
	D	7.8	417	E1-4	
Al26	C	8.4	504	E1-4	
	D	8.4	434	E1-4	
Al27	F	6.1	312	E1-4	
	G	6.1	310	E1-4	

* Garnet/Amphibole-Fe/Mg-exchange thermometry (Graham and Powell, 1984)

Seno Arcabuz shear zone

The garnet-mica schist (sample THC97) is a typical rock of the SASZ. A combination of its primary assemblage of quartz-oligoclase-muscovite-biotite-garnet, its coarse-grained primary fabric, the inverse zonation of garnet (increasing Mn, decreasing X_{Mg} from an unzoned core towards the rim) and the presence of muscovite suggests that the rock formed at high temperature, but relatively low pressure. P-T data derived by calculating multivariant equilibria E5–E8 (Tables 2 and 3) involving rim compositions of garnet and biotite range between 4.9–6.5 kbar, 578–690 °C. Due to the inverse (retrograde) zonation at the garnet rims these data do not represent P-T data at the temperature maximum, but rather suggest a stage during slow cooling after an equilibration at peak conditions at higher temperature. Furthermore calculations involving biotite and garnet core compositions yielded unreasonably high temperatures (>800 °C) showing that biotite already re-equilibrated completely by intracrystalline diffusion during cooling relative to the garnet cores. The garnet mica-schist, as well as amphibolite lenses enclosed in it, was strongly deformed at low temperature resulting in ductile deformation of quartz and brittle deformation of feldspar. Newly grown sericitic phengite in both rock types suggest elevated pressure during the retrograde P-T path.

The orthogneiss of trondhjemitic composition (sample Al 12), associated with the garnet amphibolite, has a primary predominant assemblage of quartz-plagioclase-muscovite-biotite. Its coarse grain size suggests that crystallization of the gneissose fabric occurred at elevated temperatures, which were presumably equivalent to those derived from the garnet mica-schist. The presence of muscovite points to relatively low pressures, but the temperatures were still in the stability field of muscovite + quartz. Calculation of a multivariant reaction with biotite and a theoretical potassic feldspar (E9; Table 2) results in a minimum pressure around 5.1 kbar (at 500 °C) at the upper pressure limit of the conditions derived from the garnet mica-schist (Fig. 6; Table 3).

The second fine-grained assemblage quartz-phengite-stilpnomelane-chlorite-epidote-albite grew late during the mylonitic deformation of the rock. The position of the reaction $\text{stilpnomelane} + \text{phengite} = \text{biotite} + \text{chlorite} + \text{quartz} + \text{H}_2\text{O}$, calculated by *Massonne and Szpurka (1997)*, sets an upper temperature limit of approximately 350 °C (at 6.5 kbar; Fig. 6) for the low temperature assemblage, whereas the lower limit of quartz recrystallization at 270 °C gives a lower temperature limit. Calculation of a multivariant equilibrium with chlorite and a theoretical potassic feldspar (E10; Table 2) gives a minimum pressure at 5.7 kbar (at 300 °C). The derived conditions are close to those prevailing during the retrograde shear activity within the SASZ (Fig. 6).

The spessartine-Mg-riebeckite quartzite, which occurs at the boundary between the blueschist and amphibolite areas shows a similar low grade deformational overprint as the rocks of the Seno Arcabuz shear zone and also a similar sequence of assemblages, i.e. a LP/HT assemblage followed by a retrograde HP/LT assemblage. Peak temperatures for this rock are intermediate between those of the blueschist and the amphibolite (464–505 °C; Table 3). Similar to the orthogneiss only minimum pressures (7.8–8.6 kbar at 460 °C) could be calculated with a theoretical potassic feldspar (equilibrium E11; Table 2). Reactions involving garnet and biotite

Table 4. Apatite and zircon fission-track data tabulated according to IUGS recommendations (Hurford, 1990)

Sample no.	Rock type (Unit)	Mineral	No. of crystals	Track density ($\times 10^6 \text{ tr cm}^{-2}$)		Age dispersion (P_X^2)	Central age (Ma) ($\pm 1\sigma$)	Apatite mean track length ($\mu\text{m} \pm 1 \text{ s.e.}$) (no. of tracks)	Standard deviation (μm)
				ρ_s (N_s)	ρ_d (N_d)				
AL12	Orthogneiss (SASZ)	zircon	20	7.431 (2545)	2.993 (1025)	<0.01% (99.1%)	60.9 \pm 2.7	–	–
AL16	Protomylonite (DAMC)	apatite	12	0.0788 (44)	1.384 (772)	<0.01% (99.8%)	10.8 \pm 1.7	14.26 \pm 0.76 (7)	1.86
THC96	Granodiorite (SPB)	zircon	4	4.573 (120)	1.486 (39)	<0.01% (96.7%)	84.3 \pm 15.7	–	–
		apatite	20	0.0961 (43)	1.263 (565)	<0.01% (99.0%)	18.3 \pm 3.0	14.23 \pm 0.20 (53)	1.41
THC97	Orthogneiss (SASZ)	zircon	20	10.06 (4028)	4.257 (1705)	5.97% (23.2%)	64.9 \pm 2.7	–	–
		apatite	23	0.2124 (137)	2.772 (1788)	64.79% (<0.01%)	18.5 \pm 1.8	14.54 \pm 0.23 (39)	1.44
THC126	Granodiorite (SPB)	zircon	20	3.915 (4617)	1.150 (1356)	18.24% (<0.01%)	85.4 \pm 5.0	–	–
THC127	Granite Porphyry (SPB)	zircon	20	9.866 (3992)	2.810 (1137)	3.59% (48.8%)	89.7 \pm 3.9	–	–
THC128	Granodiorite (SPB)	zircon	7	24.43 (1788)	6.039 (442)	<0.01% (88.5%)	102.8 \pm 6.1	–	–
THC129	Biotite-Granite (SPB)	zircon	10	9.124 (3213)	2.198 (774)	0.01% (76.3%)	105.2 \pm 5.0	–	–
		apatite	20	0.1628 (78)	1.611 (772)	<0.01% (99.8%)	24.7 \pm 3.1	13.53 \pm 0.18 (64)	1.39
THC160	Granodiorite (SPB)	zircon	20	6.888 (6088)	1.465 (1295)	10.00% (3.9%)	110.8 \pm 5.1	–	–
		apatite	20	0.5345 (358)	2.462 (1649)	0.01% (95.0%)	47.0 \pm 3.3	14.21 \pm 0.15 (100)	1.49

Notes: (i) analyses by external detector method using 0.5 for the $4\pi/2\pi$ geometry correction factor; (ii) ages calculated using dosimeter glass; CN5 with $\zeta_{\text{CN5}} = 358.8 \pm 12.7$; CN2 with $\zeta_{\text{CN2}} = 130.7 \pm 2.8$. (iii) P_X^2 is the probability of obtaining a X^2 value for v degrees of freedom where $v = \text{no. of crystals} - 1$; (iv) SASZ Seno Arcabuz Shear Zone; DAMC Diego de Almagro Metamorphic Complex; SPB South Patagonian Batholith

did not yield reasonable results due to significant incorporation of Mn-components in these minerals. Current activity models are not sufficiently adjusted for these additional components. The second assemblage of stilpnomelane-phengite-quartz formed at a lower temperature, which is also evident from the composition of its fine-grained white mica relative to that of the coarse muscovite of the first generation, in particular because of the depletion of Na, Ba and Ti and the greater abundance of Mn in WM II (see above). Minimum pressures of approximately 5.5 kbar (at 300 °C) can be derived for the formation of the second assemblage, when calculated with a theoretical potassic feldspar (equilibrium E12; Table 4).

The rocks of the SASZ were strongly deformed by a retrograde mylonitic deformation reflecting the inverse sinistral strike-slip activity of the shear zone (*Olivares et al.*, 2003) and represent continental crust that was originally metamorphosed under elevated temperatures, but relatively low pressures. Low temperature assemblages formed at a midcrustal level due to incorporation of these rocks in low temperature ductile shear zones resulting in recrystallisation and new mineral growth in equilibrium with changed P-T conditions.

Geochronological results

Fission track ages

Two zircon and two apatite fission track (FT) ages obtained from HP-LT rocks along the Seno Arcabuz shear zone, and two apatite and six zircon FT ages from granitoid rocks of the south Patagonian batholith, east of the Seno Arcabuz shear zone, are presented in Table 4 according to IUGS recommendations (*Hurford*, 1990). The geographical distribution of all ages is shown in Fig. 1. Fission tracks in both apatite and zircon shorten or anneal with increased temperature and duration of heating. For apatite, experimental and borehole data (*e.g.* *Green et al.*, 1989; *Ketcham et al.*, 1999) show that over geological time tracks begin to anneal at a sufficient rate to be measurable above ca. 60 °C, with complete annealing and total resetting of the apatite fission-track age occurring at between 100 °C and 120 °C. This range of temperatures is usually labelled the apatite fission-track partial annealing zone (APAZ). For samples that have undergone moderate to fast cooling, a value of 100 ± 20 °C can reasonably be assumed for the closure temperature of fission tracks in apatite. Annealing of fission tracks in pristine zircon over geological time begins at about 250 ± 20 °C, with total resetting occurring above about 310 ± 20 °C (*Tagami et al.*, 1998). These temperatures may be lower in zircons with high accumulated radiation damage (*Brandon et al.*, 1998). This translates into a closure temperature at moderate to fast cooling rates of 280 ± 30 °C for fission tracks in zircon (*Stöckhert et al.*, 1999).

Individual sample FT ages are determined by calculating the ‘central age’ (*Galbraith and Laslett*, 1993) of up to 20 individual grain ages from each sample. The central age is the population geometric mean age, while the quoted age dispersion in Table 4 (in %) is a measure of the spread in individual grain ages such that 95% of the sample grain ages will be in the range: $\exp(\log 100) \pm 2 \times (\text{age dispersion})$, with the age dispersion expressed as a proportion of 1 (i.e. an age dispersion of 15% = 0.15): the higher the age dispersion, the greater the variation

between individual grain ages. The individual grain age data for some of the zircon FT analyses are represented in histograms and probability density curves in Fig. 7. Those samples with less than 8 grain ages were not plotted.

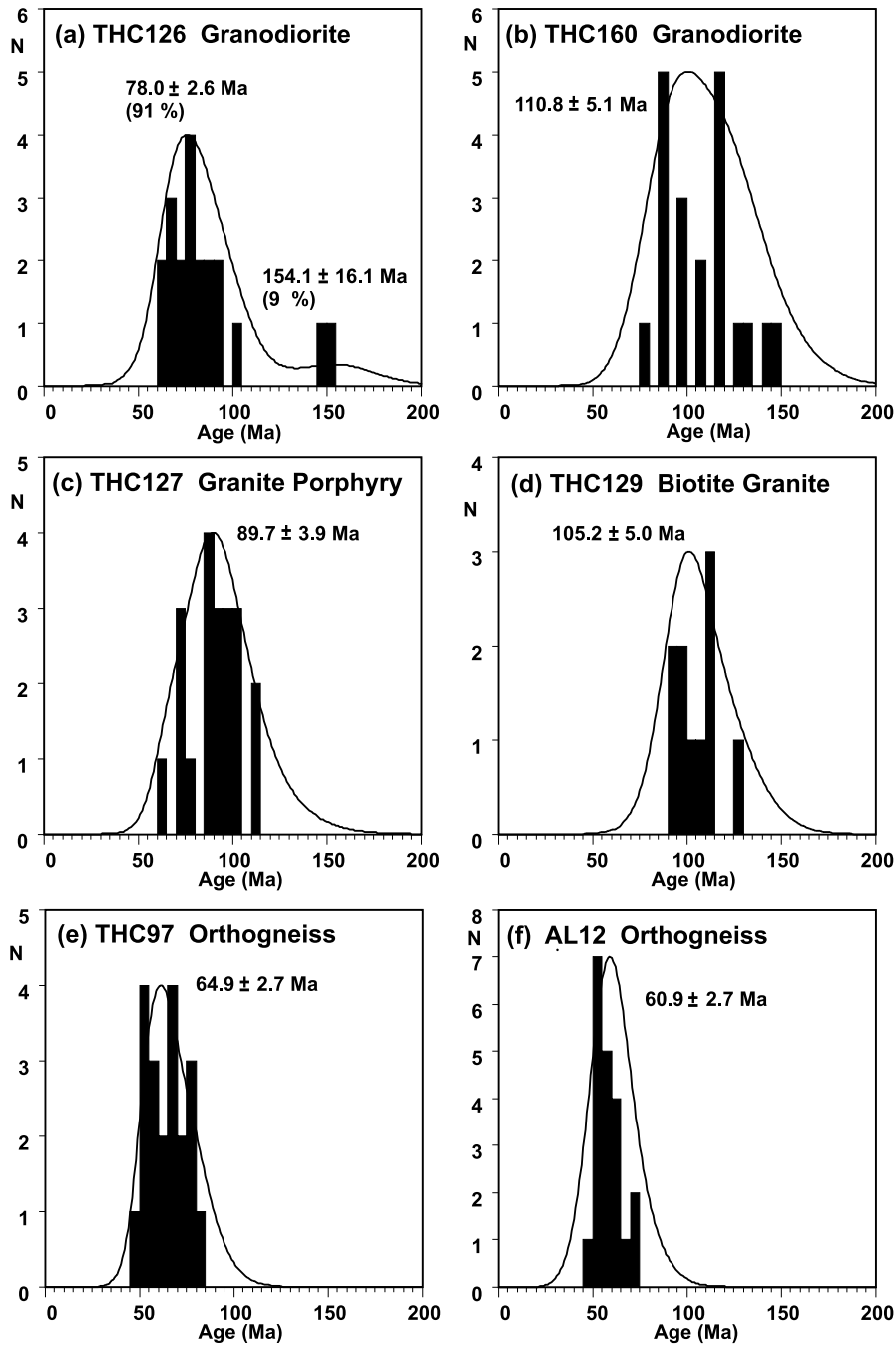


Fig. 7. Individual zircon fission-track grain age data. Data from samples THC96 and THC128 are not shown due to their low number of individual grain ages (4 grains and 7 grains respectively). Note that the individual uncertainty on each individual grain age is not shown in the histogram bars

The first four samples (Fig. 7a–d) represent samples from the South Patagonian batholith. Two of these samples (THC126 and THC160) show a mixture of individual grain ages. For sample THC126 two distinct age populations were able to be decomposed using the mixture modelling approach described by *Sambridge* and *Compston* (1994). Such a spread in ages in a single source plutonic rock can best be explained by the partial resetting of older zircon FT cooling ages – representing the Early Cretaceous intrusion and crystallization age of the sample – by reheating to temperatures of partial zircon FT annealing ($250 \pm 20^\circ\text{C}$ to $310 \pm 20^\circ\text{C}$) caused by nearby Late Cretaceous magmatism. Why the fission tracks in some zircon grains are more easily annealed than in others is not addressed here. There are several possible explanations including variable chemical composition and differences in accumulated radiation damage. What is important with regard to this study is that the rocks of the Patagonian batholith must have been at upper crustal temperatures below $250 \pm 20^\circ\text{C}$ at least since ca. 78 ± 2 Ma (sample THC126) or even earlier for other samples, e.g. sample THC129 with its apparent zircon FT cooling age of 105 ± 5 Ma.

Zircon FT ages were also obtained from two samples within the SASZ (ortho-gneiss sample AL12 and mica-schist sample THC97). Both ages (61 ± 3 and 65 ± 3 Ma, respectively; Fig. 7e, f) show single grain age populations with low age dispersion indicative of cooling ages, implying that the orthogneiss within the Seno Arcabuz shear zone cooled through $280 \pm 30^\circ\text{C}$ at least 20 Ma, and in some cases 40 Ma, after the rocks of the neighbouring South Patagonian batholith.

The individual grain age data for some of the apatite FT analyses are represented in Fig. 8. Of most relevance to the cooling of the DAMC are the data from the garnet mica-schist within the SASZ (THC97). This sample clearly contains two individual grain age populations: a dominant population with an age of 12.4 ± 1.5 Ma and three older grains that combine to give a central age of 54.7 ± 8.2 Ma. In a similar manner to the mixed zircon FT ages, this age pattern is most easily explained by re-heating to temperatures close to the upper limit of track stability in apatite over geological time (ca. $110 \pm 10^\circ\text{C}$) that was sufficient to completely reset the FT age in some grains, while others remained largely unaffected. The reheating must have occurred some time before the ca. 12 Ma cooling ages represented by the younger apatite age population. *Green* et al. (1986) indicated that fission tracks in Cl-rich apatites can be more resistant to annealing than tracks in fluorapatites with low Cl. Although the crystal chemistry of the apatites in this study was not analysed, the older ages from sample THC97 are most probably Cl-rich apatites, with the ages of these grains representing an earlier phase of rapid cooling from much higher temperatures. If the errors on the closure temperatures of the apatite and zircon fission-track system are considered, then the zircon FT age of the same sample (64.9 ± 2.7 Ma) and the older apatite FT age component imply a minimum cooling rate of $6.2^\circ\text{C}/\text{Ma}$ between ~ 68 Ma and 47 Ma. The reheating seen in sample THC97 was clearly sufficient to totally reset the apatite FT age in all the grains of sample AL16, a protomylonite (spessartine-Mg-riebeckite quartzite) further to the west within the DAMC. Two apatite FT ages from batholithic rocks directly to the east of the SASZ (THC96 and THC129) are possible to interpret in two ways. Both show older statistically single grain age populations (18 ± 3 and 25 ± 3 Ma, respectively) and relatively

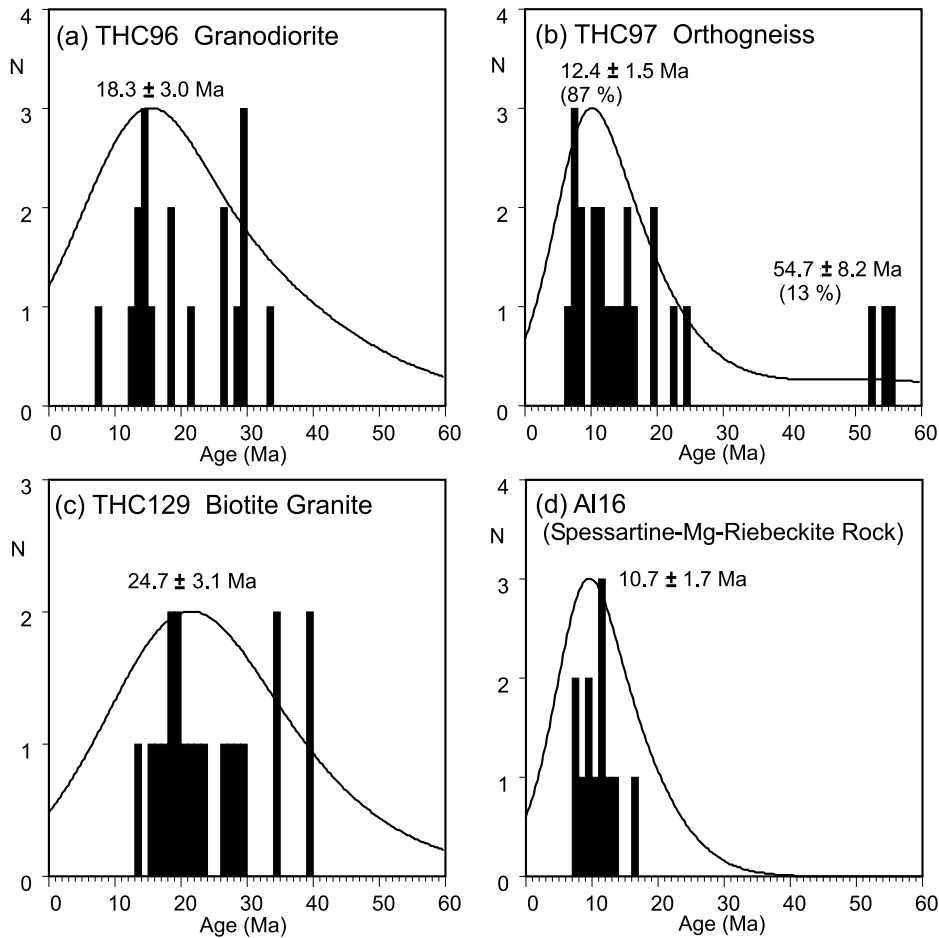


Fig. 8. Individual apatite fission-track grain age data

long, negatively skewed confined track length distributions apparently indicative of slow cooling through the APAZ. However, partial resetting could also produce such data. The large uncertainties on the single grain ages ($>50\%$) caused by their low track count (low uranium concentration) disguise a wide grain age variation between ca. 40 and 8 Ma typical of samples that have undergone partial resetting. Determination of the true thermal history of the batholithic rocks from which these two samples were taken (i.e. to reduce the uncertainty on the individual grain ages) would require apatite samples with higher track densities. Finally, batholith sample THC160 gives an apatite single population grain FT age of 47 ± 3 Ma. The corresponding long mean track length of this sample ($14.21 \mu\text{m}$), demonstrates that this sample cooled quickly to temperatures below ca. 60°C at the time represented by the apatite FT age. Interestingly, this is similar to the older apatite age component in the orthogneiss sample THC97, and suggests that these two samples, despite their different geology, shared a common sub-ca. 120°C cooling history, and were hence juxtaposed at a similar crustal level by the middle Eocene.

Table 5. Results of K–Ar geochronology

Sample	Rock type	Locality	Analysed mineral	K %	Error	Ar ⁴⁰ * 10 ⁻⁶ ccSTP/g	Ar _{Atm} %	Age Ma	Error Ma
DA2	granodiorite	Isla Contreras	amphibole	1,050		5,61	16,80	132,60	6,00
DA17	granodiorite	Isla Contreras	amphibole	0,519	1,893	2,80	28,55	133,79	7,22
DA51	garnet mica-schist	Puerto Errázuriz	muscovite	7,364	1,332	36,14	14,67	122,19	4,61
DA37	amphibolite	Caleta Lázaro	amphibole	0,284	0,500	1,34	89,99	117,50	28,43

K/Ar ages

We further present four K–Ar ages of samples (Table 5; Fig. 1) collected during the first expedition to Diego de Almagro Island in 1979 by *Mpodozis*. Although already dated in 1985, these results were never published. Two granitoid samples from exposures of the South Patagonian batholith (DA2, DA17) on Isla Contreras slightly south of the study area yield K–Ar amphibole ages of 132.6 ± 6 Ma and 133.8 ± 7.2 Ma respectively. We interpret these ages as an approximation to the age of intrusion. The K–Ar age of an amphibole of an amphibolite sample (DA37) in the DAMC is 117.5 ± 28.4 Ma. Considering the peak metamorphic temperatures of 459–565 °C reached by the amphibolite and the mean closure temperature of 500 °C for the K–Ar system in amphibole, the age can be regarded as a formation age and can approximate the age of the peak of HP-metamorphism. Finally, a mica-schist sample (DA 51), located in the SASZ, yields a K–Ar age of muscovite of 122.2 ± 4.6 Ma. Considering the peak temperature of 578–690 °C reached by this rock and the mean closure temperature of the K–Ar system in white mica, this age is interpreted as a cooling age after the peak of the HT-metamorphism that overprinted the rocks of the SASZ prior to the shear event.

Discussion and geodynamic constraints

Combining the geochronological data with the derived set of interrelated and converging P–T paths and the structural data by *Olivares et al.* (2003) allows to reconstruct the evolution of the DAMC and its emplacement against very low grade retrowedge complexes towards the east along the SASZ during Mesozoic times (Fig. 1B, 9).

The collage of metamorphic complexes and their protoliths

So far we have no information on the age or nature of the protoliths of the DAMC, which represent the fossil accretionary prism due to the HP/LT metamorphism of its rocks. In analogy to other accretionary systems in the basement of the Chilean Cordillera (e.g. *Hervé*, 1988) it could be composed of a mixture of continent-derived greywackes and slices of oceanic crust. However, the spessartine-Mg-riebeckite quartzite at the boundary between the blueschist and amphibolite areas

yielded uniform U/Pb single grain zircon ages of 157 ± 2 Ma (SHRIMP; *Hervé and Fanning, 2003*) suggesting a rhyolite or rhyolitic tuff as protolith. It was presumably coeval with the widespread Middle to Late Jurassic “Tobifera” acid igneous event in Patagonia further to the east (*Pankhurst and Rapela, 1995*). A similar continental crustal origin can be attributed to the HT metamorphic rocks of the SASZ. SHRIMP U-Pb dating of zircon in the orthogneiss of the SASZ reveals that its magmatic rims formed at ~ 170 Ma, whereas its cores show a great diversity of older inherited ages (*Hervé and Fanning, 2003*). Rocks, whose LP/HT evolution is comparable with the rocks of the SASZ, occur further S in the Cordillera Darwin ($54^{\circ}30' S$) and were exhumed around 70–80 Ma (*Kohn et al., 1993*). These few known protolith ages are distinctly younger than the sedimentation age of the very low grade Duque de York Complex in the east, which does not yield igneous zircons younger than late Early Permian in the source area (*Hervé et al., 2003*). The Duque de York Complex in turn is overlying obducted oceanic crust with Upper Carboniferous-Lower Permian sediments (*Forsythe and Mpodozis, 1983*) and constitute a very low grade retrowedge area, which was intruded by the South Patagonian batholith.

A Jurassic paired metamorphic belt

Our amphibole K–Ar age of 117.5 ± 28.4 Ma may approximate the local age of peak metamorphic conditions in the amphibolite in the eastern part of the DAMC. Metamorphism evidently occurred within an accretionary prism approximately coeval with the intrusion of the South Patagonian batholith, which formed the magmatic arc: An age range of 69–149 Ma for the emplacement of plutonites of the South Patagonian Batholith to the N and S of Diego de Almagro Island was derived by *Weaver et al. (1990)* and *Bruce et al. (1991)*. Our K–Ar ages of 132.6 ± 6 Ma and 133.8 ± 7.2 Ma of amphibole in granodiorite fall within this age range. The metamorphic rocks of the SASZ reveal a LP/HT-metamorphism around 4.9 kbar, 580–630 °C presumably related to heat advection within the magmatic arc. Our muscovite K–Ar age of 122.2 ± 4.6 Ma obtained from the garnet mica-schist of the SASZ presumably relates to cooling after this HT-metamorphic event. This cooling age is corroborated by ^{40}Ar – ^{39}Ar ages in a white mica fish within the orthogneiss of the SASZ ranging between 136 ± 8 to 120 ± 8 Ma (*Olivares et al., 2003*). Hence the existence of a true contemporaneous, paired metamorphic belt during Jurassic times is suggested.

Two contrasting HP/LT areas in the DAMC

Peak metamorphic conditions (stage I) in the blueschist intercalations are recorded at 9.5–13.5 kbar, 380–450 °, whereas in the amphibolite lenses the same stage was reached at 11.2–13.2 kbar, 460–565 °C. This indicates that the two contrasting HP areas were subducted to similar depth, but submitted to distinctly different peak temperatures recording different metamorphic gradients in the accretionary wedge, i.e. approximately within the range of 8–13 °C/km for the blueschist and 10–14 °C/km for the amphibolite (on the basis of an average

density of 2.8 g/cm^3). Gradients $>10 \text{ }^\circ\text{C/km}$ appear relatively high for an accretionary prism, but seem to be typical for the entire basement of the Chilean Coastal Cordillera in general (Willner et al., 2000, 2001, 2004). Such high gradients may indicate relatively slow subduction and/or a moderately inclined slab according to numerical modeling (Peacock, 1996). Hence variation of the slab geometry might have caused the difference of the recorded gradients. On the other hand, the amphibolite area could have had a different position within the accretionary wedge and should have been metamorphosed nearer to the hot mantle wedge under the adjacent continent (Fig. 9). As a result it was exhumed very close to the non-subducted retrowedge area. A similar setting was also observed by Trouw et al. (1998) in the Cretaceous accretionary wedge of Elephant Island (South Shetland Islands, Antarctica), which could be a close time-equivalent of the DAMC along a once common convergent margin (Willner et al., 1999). The

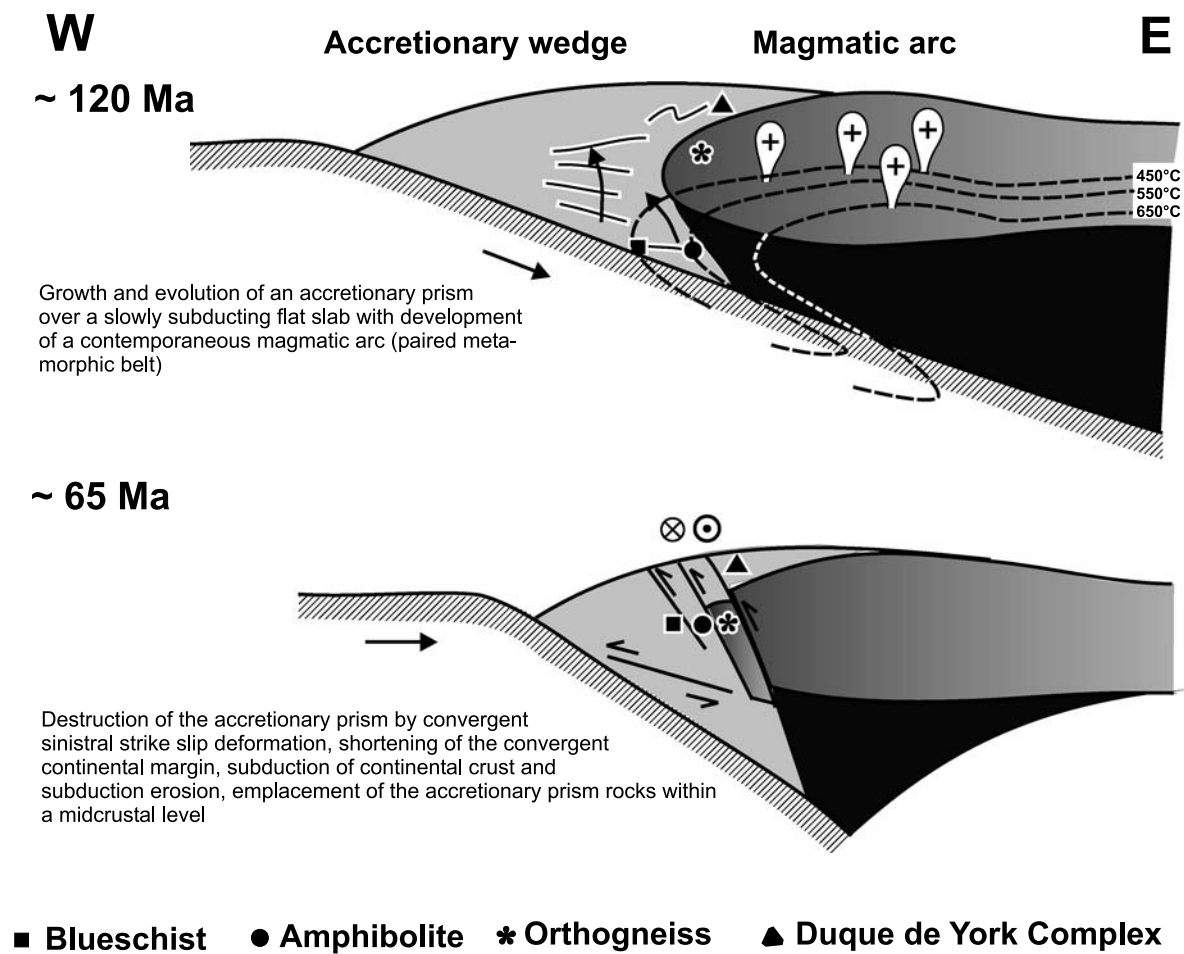


Fig. 9. Conceptual model for the development of the convergent margin of southernmost Chile during the Mesozoic

position of the highest grade rocks of the accretionary prism near to the very low grade rocks of the retrowedge in transition to the backstop system is also common for the basement of the Chilean Coastal Cordillera (*Willner et al.*, 2000, 2004; *Kato*, 1985). Hence this setting reveals a clear polarity of the direction of subduction (*Trouw et al.*, 1998). The observed difference in metamorphic gradient in the study area may also be explained by isobaric heating at maximum depth. This would require a mechanism, which allows horizontal particle movement after accretion and before vertical exhumation, crossing isotherms towards higher temperatures. Recent analogue modeling of accretionary wedges with sandbox experiments (*Kukowski et al.*, 2002) has shown that basal accretion may involve formation of weakly inclined basal duplexes resulting in an early subhorizontal particle path after accretion.

Exhumation and emplacement of the DAMC

During the early retrograde P-T path in both metabasites recrystallization and new mineral growth under static conditions and partly fluid infiltration caused local equilibria (stage II) at 6.3–9.6 kbar, 320–385 °C in the blueschist and 6.1–8.4 kbar, 310–505 °C in the amphibolite. Both recorded partial P-T paths are clockwise and end at similar P-T conditions at ~6–7 kbar, 300–350 °C in the stability field of stilpnomelane + phengite, i.e. they converge within a midcrustal level. These conditions were also approximated for the retrograde assemblages of the LP/HT rocks (orthogneiss, garnet mica-schist, amphibolite) in the SASZ and of rocks at the boundary between the blueschist and amphibolite areas (spessartine-Mg-riebeckite quartzite). These retrograde assemblages recrystallized during and at the end of ductile shearing with convergent sinistral strike slip kinematics (*Olivares et al.*, 2003). This suggests that the observed juxtaposition at a midcrustal level, which involved HP/LT rocks of the accretionary prism represented by the DAMC and rocks of continental crust with a LP/HT imprint within the SASZ, was related to the convergent strike slip activity along SASZ. The metamorphic gradient during this process (~10–14 °C/km) was comparable to the one reflected by the peak metamorphic conditions in the metabasite of the DAMC. The high pressure rocks of the DAMC had probably already reached midcrustal levels via an independent exhumation process.

Fission track ages of zircon in the orthogneiss and the garnet-mica schist of 61 ± 3 and 65 ± 3 Ma respectively indicate cooling through 280 ± 30 °C and hence date the end of the shearing activity in the SASZ, but also the age of convergence of the rocks of the DAMC and the SASZ at a midcrustal level. A prolonged earlier history of the shear zone is indicated by $^{40}\text{Ar}/^{39}\text{Ar}$ ages of masses of smaller, recrystallized white mica aggregates in deformed domains at 89 ± 8 Ma (*Olivares et al.*, 2003).

Considering the age of the peak of the high pressure metamorphism in the amphibolite and the age of the convergence at the midcrustal level as time markers, an approximate minimum average exhumation rate of ~0.30–0.45 mm/a and a cooling rate of ~2–4 °C/Ma may be estimated for the partial retrograde P-T path recorded by the amphibolite of the DAMC. Such rates would be compatible with

average erosion rates. Erosion can be the principal unroofing process controlling exhumation in accretionary prisms, as demonstrated by *Ring and Brandon (1999)* for the Franciscan. However, the HP rocks might have resided for a considerable amount of time at midcrustal levels before the shear event. The retrowedge area to the east of the SASZ, which includes the South Patagonian batholith, cooled much earlier through the $280 \pm 30^\circ\text{C}$ isotherm at 105–78 Ma, according to zircon FT ages from the granitoids. The very low grade complexes of the retrowedge area and the shallow intrusion level of the South Patagonian batholith indicate little crustal thickening within the magmatic arc.

The fission track age of 54.7 ± 8.2 Ma in a sub-population of apatites in the orthogneiss of the SASZ can be interpreted as representing cooling of these rocks to below $110 \pm 10^\circ\text{C}$. This further cooling of about 150°C and exhumation to a near-surface level after the end of the shear activity implies an increase of mean exhumation to about 2 mm/a and cooling rates to at least $6.2^\circ\text{C}/\text{Ma}$ (see above) and likely much higher during this second exhumation period. Such increased rates are probably related to a local increase in crustal thickness following the convergent shear event, resulting in significant relief. These rates are also compatible with erosion rates and could have been enhanced by a humid climate. Nevertheless, normal fault kinematics were also reported in the SASZ by *Olivares et al. (2003)*. A similar maximum apatite FT age in one granitoid of 47 ± 3 Ma is further indication that the rocks of the SASZ and the DAMC reached a near-surface level during the Eocene and their position relative to the very low grade complexes of the retrowedge area and the presently exposed level of the South Patagonian batholith. The whole area was partially reheated up to $110 \pm 10^\circ\text{C}$ some time before about 12 Ma.

Summarizing, the fossil accretionary prism was modified by convergent strike slip shearing at a midcrustal level under a low geothermal gradient during exhumation of high pressure rocks of the DAMC. This event caused (1) substantial late shortening of the continental margin, (2) telescoping and amalgamation of different portions of the accretionary system and the adjacent continental margin and (3) subduction of continental crust. The latter is a rather rare process at a convergent continental margin. The same event is probably related to “subduction erosion” of lost outer parts of the accretionary prism (e.g. the very low grade frontal accretion zone) that originally extended beyond the Pacific coast. The destruction of the accretionary prisms also marks the end of subduction mass flow and accretion at this latitude of the South American convergent margin.

Acknowledgements

This research was supported by Fondecyt projects 1980741/1010412 and the Cátedra Presidencial de Ciencias granted to *FH*, a DFG-grant (Wi875/8-1,2) to *AW* and the German-Chilean BMBF-CONICYT cooperation project Chl 01A 6A “High pressure metamorphic rocks in Chile”. Reviews by *R. Spikings* and *K. Stüwe* as well as careful editorial handling by *J. Raith* considerably improved the manuscript. We also thank *H.-J. Bernhardt* for providing the microprobe facilities in Bochum. This study is also a contribution to IGCP 436 “Pacific Gondwana Margin”.

Appendix: Representative mineral compositions

	Al17		Al21		Al22		Al25		Al26		Al27		THC97		Al12		Al16	
	I	II	I	II	I	II	I	II	I	II	I	II	I	II	I	II	I	II
SiO ₂	50,85	46,91	49,52	47,52	49,10	48,48	50,15	48,20	50,96	48,47	52,21	48,79	45,85	46,78	45,83	50,77	44,50	51,51
TiO ₂	0,04	0,47	0,23	0,16	0,34	0,37	0,18	0,24	0,05	0,20	0,29	0,07	0,74	0,30	1,08	0,01	0,59	0,05
Al ₂ O ₃	24,71	29,28	26,67	24,78	26,31	27,60	25,35	25,42	24,91	26,13	26,48	25,44	35,08	29,65	32,35	25,59	29,82	19,78
Cr ₂ O ₃	0,01	0,04	0,08	0,09	0,00	0,00	0,03	0,05	0,05	0,06	0,13	0,08	0,01	0,00	0,00	0,01	0,00	0,00
FeO	3,73	4,35	3,49	6,78	5,07	4,71	3,63	5,16	4,35	4,98	3,23	5,13	1,57	3,01	1,90	4,04	5,13	6,49
MnO	0,03	0,01	0,00	0,13	0,03	0,04	0,05	0,00	0,04	0,05	0,05	0,08	0,00	0,01	0,05	0,06	0,07	0,21
MgO	3,60	2,01	3,13	3,09	2,77	2,59	3,44	2,96	3,26	2,82	3,42	4,10	0,88	2,29	1,36	2,73	1,17	4,22
BaO	0,24	0,11	0,26	0,28	0,18	0,43	0,13	0,23	0,18	0,23	0,12	0,00	nd	nd	0,48	0,29	1,80	0,01
Na ₂ O	0,15	1,26	0,53	0,18	0,42	0,80	0,30	0,35	0,12	0,27	0,18	0,09	1,29	0,60	0,36	0,11	0,30	0,05
K ₂ O	11,06	9,44	10,10	10,81	11,08	10,64	11,08	10,82	11,26	10,61	11,04	10,20	9,39	10,48	10,82	11,08	10,43	11,49
H ₂ O ¹	4,33	4,34	4,37	4,28	4,35	4,37	4,36	4,27	4,41	4,35	4,56	4,43	4,50	4,36	4,40	4,41	4,21	4,19
Sum	98,75	98,22	98,38	98,10	99,65	100,03	98,70	97,70	99,59	98,17	101,71	98,41	99,31	97,48	98,63	99,10	98,02	98,00
Si	6,935	6,418	6,744	6,586	6,693	6,583	6,855	6,695	6,922	6,674	6,867	6,607	6,114	6,440	6,244	6,910	6,25	7,185
Al ^{IV}	1,065	1,582	1,256	1,414	1,307	1,418	1,145	1,305	1,078	1,326	1,133	1,393	1,886	1,560	1,756	1,091	1,754	0,815
Al ^{VI}	2,908	3,139	3,025	2,634	2,920	2,998	2,940	2,858	2,909	2,914	2,972	2,667	3,628	3,250	3,439	3,014	3,183	2,436
Cr	0,001	0,004	0,008	0,010	0,000	0,000	0,003	0,006	0,005	0,006	0,014	0,009	0,002	0,000	0,000	0,001	0	0,000
Ti	0,004	0,048	0,023	0,017	0,035	0,038	0,018	0,025	0,005	0,020	0,029	0,007	0,075	0,031	0,111	0,001	0,063	0,005
Fe ²⁺	0,426	0,361	0,397	0,265	0,469	0,415	0,415	0,421	0,494	0,423	0,355	0,077	0,175	0,048	0,217	0,459	0,453	0,588
Fe ³⁺	0,000	0,137	0,000	0,521	0,109	0,121	0,000	0,178	0,000	0,151	0,000	0,504	0,000	0,298	0,000	0,000	0,147	0,170
Mn	0,003	0,001	0,000	0,016	0,004	0,005	0,006	0,000	0,005	0,006	0,006	0,009	0,000	0,001	0,006	0,007	0,008	0,024
Mg	0,733	0,411	0,635	0,638	0,564	0,524	0,702	0,612	0,659	0,580	0,670	0,828	0,174	0,471	0,276	0,554	0,244	0,878
Ba	0,013	0,006	0,014	0,015	0,009	0,023	0,007	0,012	0,009	0,013	0,006	0,000	nd	nd	0,025	0,015	0,099	0,000

(continued)

Appendix (continued)

	A1 White Mica																	
	Al17		Al21		Al22		Al25		Al26		Al27		THC97		Al12		Al16	
	I	II	I	II	I	II	I	II	I	II	I	II	I	II	I	II	I	II
Na	0,040	0,334	0,140	0,047	0,112	0,209	0,079	0,094	0,032	0,071	0,046	0,024	0,334	0,161	0,094	0,030	0,083	0,014
K	1,925	1,648	1,755	1,911	1,926	1,842	1,933	1,917	1,951	1,864	1,852	1,762	1,597	1,839	1,880	1,924	1,866	2,040
OH	4,000	4,000	4,000	4,000	4,000	4,000	4,000	4,000	4,000	4,000	4,000	4,000	4,000	4,000	4,000	4,000	4,000	4,000
X _{Ms}	0,460	0,508	0,482	0,476	0,496	0,487	0,475	0,485	0,469	0,513	0,491	0,502	0,705	0,622	0,726	0,496	0,621	0,306
X _{MAC}	0,300	0,113	0,233	0,213	0,192	0,169	0,271	0,210	0,267	0,199	0,287	0,278	0,029	0,134	0,076	0,253	0,060	0,355
X _{FAC}	0,174	0,099	0,146	0,089	0,160	0,134	0,160	0,144	0,200	0,145	0,152	0,026	0,029	0,085	0,059	0,210	0,112	0,237

The proportion of cations is based on 42 valencies neglecting the interlayer cations; the sum of octahedrally coordinated cations is set at 4.1 to allow for an estimation of Fe³⁺; the amounts of Cl and F are near or below detection limit; ¹ amount calculated; *nd* not determined; symbols: *Ms* muscovite, *MAC* Mg-aluminoceladonite, *FAC* Fe-aluminoceladonite

	A2 Biotite												
	Garnet						Garnet						
	Al12		Al16		THC97		Al16		Al21		Al27		THC97
I	II	I	II	I	II	core	rim	core	rim	core	rim	core	rim
SiO ₂	32,96	34,68	38,70	35,42	SiO ₂	36,19	36,41	36,92	36,94	38,63	39,07	36,73	36,73
TiO ₂	2,70	2,39	0,44	2,15	TiO ₂	0,05	0,02	0,06	0,06	0,27	0,00	0,03	0,03
Al ₂ O ₃	15,19	13,90	14,10	18,30	Al ₂ O ₃	20,43	20,39	20,59	20,67	21,64	21,89	20,94	20,94
Cr ₂ O ₃	0,03	0,00	0,04	nd	Cr ₂ O ₃	0,01	0,06	0,18	0,04	0,11	0,11	nd	nd
FeO	24,79	23,28	19,00	19,63	FeO	19,59	19,39	19,86	20,47	25,68	25,70	35,30	35,57
MnO	0,24	0,95	0,53	0,06	Fe ₂ O ₃ ¹	0,79	1,45	1,08	0,96	0,41	0,51	0,98	0,68
MgO	7,55	8,44	11,88	9,21	MnO	17,05	16,61	9,28	7,89	1,03	0,82	2,07	2,07
BaO	0,28	1,06	nd	nd	MgO	2,25	2,74	0,75	0,74	5,57	5,65	2,84	2,84

Na ₂ O	0,02	0,02	0,01	0,41	CaO	2,36	2,67	11,11	11,66	7,65	8,09	1,93	1,93
K ₂ O	9,91	9,66	9,91	9,36	Sum	98,72	99,74	99,83	99,43	100,99	101,84	100,82	100,79
Cl	0,01	0,03	nd	0,04	Si	5,942	5,912	5,938	5,949	5,968	5,979	5,932	5,908
F	0,34	0,40	0,82	0,00	Al ^{IV}	0,058	0,088	0,062	0,051	0,033	0,021	0,068	0,092
H ₂ O ¹	3,53	3,53	3,52	3,90	Al ^{VI}	3,895	3,813	3,840	3,872	3,907	3,928	3,922	3,878
Sum ²	97,55	98,16	98,60	98,43	Cr	0,001	0,008	0,022	0,005	0,013	0,013	nd	nd
Si	5,351	5,571	5,938	5,451	Fe ³⁺	0,098	0,177	0,131	0,116	0,048	0,059	0,075	0,118
Al ^{IV}	2,649	2,429	2,062	2,549	Ti	0,006	0,002	0,007	0,007	0,031	0,000	0,004	0,004
Al ^{VI}	0,257	0,202	0,488	0,771	Mg	0,550	0,663	0,179	0,179	1,283	1,289	0,811	0,681
Cr	0,005	0,000	0,005	nd	Fe ²⁺	2,689	2,633	2,670	2,756	3,317	3,289	4,739	4,749
Ti	0,330	0,289	0,051	0,248	Mn	2,371	2,284	1,264	1,076	0,135	0,106	0,171	0,282
Fe	3,367	3,128	2,438	2,526	Ca	0,415	0,464	1,915	2,011	1,266	1,327	0,312	0,333
Mn	0,034	0,130	0,069	0,007	X _{And}	0,002	0,003	0,010	0,010	0,003	0,003	0,001	0,002
Mg	1,827	2,021	2,717	2,112	X _{uva}	0,000	0,000	0,002	0,000	0,001	0,001	0,000	0,000
Ba	0,018	0,067	nd	nd	X _{Sps}	0,394	0,378	0,210	0,179	0,023	0,018	0,028	0,047
Na	0,008	0,007	0,003	0,123	X _{Grs}	0,067	0,073	0,305	0,323	0,206	0,217	0,051	0,053
K	2,054	1,979	1,940	1,837	X _{Pyr}	0,091	0,110	0,030	0,030	0,214	0,214	0,135	0,113
Cl	0,004	0,008	nd	0,010	X _{Alm}	0,446	0,436	0,443	0,458	0,553	0,547	0,786	0,786
F	0,172	0,205	0,398	0,000	X _{Mg}	0,170	0,201	0,063	0,061	0,279	0,282	0,146	0,125
OH	3,824	3,787	3,602	3,990									

The proportion of cations is based on 44 valencies; ¹ value calculated ² sum corrected for F and Cl; *nd* not determined

The proportion of cations is based on 48 valencies, including 10 cations in the tetrahedral and octahedral site, to calculate the proportion of Fe³⁺; ¹ value calculated; symbols of garnet components after *Kretz* (1983)

Appendix (continued)

Titanite	Al14	Al15	Al17	Al22	Al25	Al26
SiO ₂	29,29	30,36	30,00	28,54	30,02	30,19
TiO ₂	38,24	39,21	37,55	38,28	37,39	37,37
Al ₂ O ₃	1,50	0,43	1,16	1,01	1,06	1,24
Fe ₂ O ₃	0,34	0,74	0,91	1,15	0,52	1,09
MnO	0,03	0,05	0,03	0,05	0,03	0,09
CaO	29,15	28,89	28,78	28,61	28,89	28,61
H ₂ O ¹	0,36	0,24	0,39	0,27	0,24	0,12
F	0,13	0,04	0,12	0,18	0,13	0,28
Sum ²	98,90	99,88	98,78	98,00	98,18	98,94
Si	0,962	0,991	0,987	0,950	0,993	0,992
Ti	0,945	0,962	0,929	0,959	0,929	0,923
Al	0,058	0,017	0,045	0,040	0,041	0,048
Fe ³⁺	0,009	0,018	0,023	0,029	0,013	0,027
Ca	1,026	1,010	1,015	1,021	1,023	1,007
Mn	0,001	0,001	0,001	0,001	0,001	0,003
F	0,035	0,024	0,038	0,026	0,024	0,012
OH	0,028	0,010	0,027	0,040	0,029	0,062
O*	4,908	4,954	4,918	4,910	4,923	4,916

Sum of cations: 3; OH = (Al + Fe³⁺) - F; ¹ value calculated; ² sum corrected for amount of F; O* = [(Σ positive valencies) - OH - F]/2; *nd* not determined; *Cl* below detection limit

Appendix (continued)

	Al14		Al15		Al16		Al17		Al21		Al22		Al25		Al26		Al27	
	I	II																
SiO ₂	41,07	46,92	42,09	52,45	53,24	51,95	56,20	50,64	55,99	53,27	54,92	48,77	53,30	51,71	53,30	51,71	45,11	54,15
TiO ₂	0,75	0,33	0,85	0,03	0,08	0,28	0,00	0,05	0,03	0,05	0,06	0,24	0,08	0,07	0,08	0,07	2,26	0,14
Al ₂ O ₃	12,91	7,56	12,94	2,40	2,75	2,46	9,80	3,48	10,36	2,03	7,53	9,58	4,48	3,43	4,48	3,43	11,73	1,44
Cr ₂ O ₃	0,09	0,02	0,04	0,00	0,02	0,00	0,00	0,00	0,07	0,01	0,01	0,01	0,00	0,00	0,00	0,00	0,11	0,07
Fe ₂ O ₃ ¹	0,29	0,00	4,73	1,08	13,35	14,17	4,29	4,72	3,94	2,61	7,50	6,03	2,93	6,58	2,93	6,58	1,97	0,10
FeO	17,82	17,57	12,26	13,98	10,83	9,63	12,13	15,04	9,40	12,96	11,17	13,86	14,24	11,34	14,24	11,34	10,64	14,08
MnO	0,27	0,38	0,30	0,20	0,70	1,12	0,15	0,39	0,03	0,41	0,04	0,26	0,24	0,20	0,24	0,20	0,07	0,20
MgO	7,70	9,97	9,87	13,63	7,46	7,96	7,23	10,66	8,88	13,30	7,74	7,84	11,03	12,14	11,03	12,14	12,13	14,42
CaO	12,19	12,37	11,05	11,65	1,11	1,86	0,38	9,56	0,87	10,53	0,54	5,75	7,62	8,87	7,62	8,87	11,23	12,45
BaO	0,00	0,05	0,00	0,00	0,02	0,01	0,02	0,02	0,05	0,01	0,05	0,01	0,06	0,06	0,06	0,06	nd	nd
Na ₂ O	1,16	0,75	2,71	1,11	6,20	5,77	6,96	2,21	6,67	1,43	6,92	4,90	3,52	2,28	3,52	2,28	1,93	0,33
K ₂ O	1,34	0,56	0,22	0,11	0,08	0,13	0,03	0,19	0,02	0,09	0,03	0,20	0,11	0,13	0,11	0,13	0,38	0,05
F	0,10	0,09	0,10	0,11	0,09	0,13	0,06	0,10	0,08	0,10	0,11	0,10	0,09	0,11	0,09	0,11	0,06	0,17
Cl	0,01	0,03	0,00	0,00	0,00	0,00	0,00	0,04	0,00	0,00	0,01	0,00	0,00	0,02	0,00	0,02	0,02	0,00
H ₂ O ¹	1,88	1,92	1,96	1,98	1,98	1,93	2,09	1,95	2,09	2,00	2,02	1,99	2,02	1,99	2,02	1,99	2,02	1,80
Sum ²	97,54	98,52	99,08	98,68	97,89	97,34	99,31	99,00	98,45	98,76	98,55	99,50	99,68	98,89	99,68	98,88	99,64	99,50
Si	6,374	7,136	6,304	7,723	7,921	7,799	7,940	7,557	7,880	7,809	7,897	7,181	7,751	7,594	7,751	7,594	6,571	7,865
Al ^{IV}	1,626	0,864	1,696	0,277	0,079	0,201	0,060	0,444	0,120	0,191	0,104	0,819	0,249	0,406	0,249	0,406	1,429	0,135
Ti	0,087	0,038	0,096	0,003	0,009	0,031	0,000	0,005	0,003	0,005	0,007	0,027	0,008	0,008	0,008	0,008	0,248	0,015
Al ^{VI}	0,737	0,491	0,589	0,140	0,402	0,235	1,571	0,169	1,597	0,159	1,173	0,843	0,519	0,189	0,519	0,189	0,585	0,110
Cr	0,011	0,002	0,004	0,000	0,003	0,000	0,001	0,000	0,008	0,002	0,001	0,001	0,000	0,000	0,000	0,000	0,013	0,008
Fe ³⁺	0,034	0,000	0,533	0,119	1,495	1,601	0,456	0,530	0,418	0,288	0,812	0,669	0,320	0,728	0,320	0,728	0,216	0,011
Fe ²⁺	2,313	2,234	1,535	1,722	1,348	1,210	1,433	1,876	1,106	1,589	1,343	1,707	1,732	1,393	1,732	1,393	1,297	1,710

(continued)

Appendix (continued)

A3 Amphibole		Al15		Al16		Al17		Al21		Al22		Al25		Al26		Al27		
	II	I	II															
Mn	0,035	0,050	0,038	0,025	0,089	0,143	0,018	0,049	0,004	0,051	0,006	0,033	0,029	0,025	0,029	0,025	0,009	0,025
Mg	1,782	2,259	2,205	2,992	1,655	1,781	1,522	2,371	1,864	2,906	1,659	1,720	2,391	2,659	2,391	2,659	2,634	3,122
Ca	2,027	2,016	1,774	1,838	0,178	0,299	0,058	1,529	0,131	1,654	0,083	0,907	1,186	1,396	1,186	1,396	1,753	1,937
Ba	0,000	0,003	0,000	0,000	0,001	0,001	0,001	0,001	0,003	0,000	0,003	0,001	0,003	0,003	0,003	0,003	nd	nd
Na	0,349	0,221	0,788	0,317	1,788	1,678	1,908	0,638	1,821	0,407	1,927	1,400	0,993	0,651	0,993	0,651	0,545	0,092
K	0,265	0,110	0,042	0,020	0,015	0,025	0,006	0,036	0,003	0,017	0,006	0,037	0,021	0,025	0,021	0,025	0,070	0,009
Cl	0,002	0,008	0,000	0,001	0,000	0,000	0,000	0,011	0,000	0,000	0,003	0,001	0,000	0,005	0,000	0,005	0,005	0,000
F	0,050	0,044	0,046	0,051	0,040	0,063	0,027	0,048	0,036	0,048	0,052	0,046	0,043	0,049	0,043	0,049	0,030	0,078
OH	1,948	1,949	1,954	1,949	1,960	1,937	1,973	1,941	1,964	1,952	1,945	1,953	1,957	1,946	1,957	1,946	1,970	1,922

The proportion of cations is based on 46 valencies and the sum of cations = 13 except for Ca, Na and K for estimation of Fe³⁺; ¹ value calculated; ² sum corrected for F and Cl

A4 Chlorite		Al15		Al17		Al21		Al22		Al25		Al26		Al27	
	II	I	II	I/II	I	II									
SiO ₂	25,90	25,81	24,82	25,14	25,92	25,58	26,12	26,02	26,31	26,04	25,23	26,97	27,24	27,24	
TiO ₂	0,08	0,04	0,03	0,03	18,91	0,03	0,03	0,03	18,90	18,87	0,04	0,00	0,40	0,40	
Al ₂ O ₃	18,24	19,05	18,82	18,27	14,99	19,37	18,35	18,11	18,04	16,59	19,34	19,74	19,82	19,82	
FeO	30,92	27,06	29,90	28,67	27,09	25,65	26,23	25,84	22,24	23,88	29,50	27,95	21,27	21,27	
MnO	0,51	0,52	0,42	0,43	0,56	0,50	0,65	0,75	0,23	0,44	0,41	0,42	0,06	0,06	
MgO	12,53	15,28	13,06	13,68	0,01	15,45	15,43	15,28	0,10	0,04	12,79	12,67	18,63	18,63	

CaO	0,01	0,04	0,00	0,16	0,03	0,02	0,01	0,03	0,02	0,03	0,03	0,03	0,19	0,23
Na ₂ O	0,00	0,00	0,00	0,04	0,05	0,01	0,01	0,00	0,02	0,05	0,01	0,07	0,07	0,02
K ₂ O	0,01	0,02	0,00	0,01	0,01	0,00	0,01	0,02	0,03	0,04	0,02	0,02	0,02	0,01
H ₂ O ¹	11,07	11,22	10,94	10,89	11,21	11,15	11,14	11,06	11,24	11,17	11,03	11,25	11,25	11,58
Sum	99,27	99,04	97,99	97,32	98,78	97,76	97,98	97,14	97,13	97,15	98,40	99,28	99,28	99,26
Si	5,612	5,504	5,439	5,517	5,544	5,490	5,617	5,639	5,558	5,574	5,483	5,731	5,731	5,604
Al ^{IV}	2,388	2,496	2,561	2,483	2,456	2,510	2,383	2,361	2,442	2,426	2,517	2,269	2,269	2,396
Al ^{VI}	2,270	2,291	2,299	2,242	2,310	2,391	2,268	2,265	2,300	2,335	2,435	2,674	2,674	2,409
Ti	0,013	0,006	0,005	0,005	0,002	0,005	0,004	0,005	0,016	0,007	0,006	0,000	0,000	0,062
Fe	5,603	4,825	5,479	5,261	4,845	4,604	4,717	4,684	3,959	4,275	5,362	4,966	4,966	3,659
Mn	0,094	0,094	0,079	0,080	0,101	0,091	0,118	0,138	0,042	0,079	0,075	0,075	0,075	0,011
Mg	4,045	4,856	4,267	4,475	4,778	4,942	4,944	4,936	5,723	5,293	4,143	4,013	4,013	5,712
Ca	0,003	0,008	0,000	0,037	0,007	0,006	0,003	0,008	0,005	0,007	0,008	0,043	0,043	0,050
K	0,002	0,006	0,001	0,002	0,003	0,001	0,003	0,005	0,009	0,011	0,005	0,006	0,006	0,003
Na	0,000	0,000	0,000	0,015	0,020	0,003	0,002	0,000	0,009	0,022	0,003	0,028	0,028	0,008
OH	16,00	16,00	16,00	16,00	16,00	16,00	16,00	16,00	16,00	16,00	16,00	16,00	16,00	16,00

The proportion of cations is based on 56 valencies; ¹ value calculated; F, Cl are at detection limit

Epidote	Al14		Al15		Al17		Al21		Al22		Al25		Al26	
	I	II												
SiO ₂	37,21	37,52	37,04	37,01	36,78	37,44	37,65	35,5	35,45	37,57	37,87	37,5	37,29	37,29
TiO ₂	0,22	0,1	0,06	0,1	0	0,14	0,15	0,03	0,1	0,19	0,15	0,03	0,16	0,16
Al ₂ O ₃	27,32	24,46	22,68	23,84	21,68	25,2	25,8	22,14	23,56	24,76	25,06	23,82	24,18	24,18
Cr ₂ O ₃	0,04	0,03	0,05	0,1	0,02	0,04	0	0	0,01	0,06	0	0,08	0,09	0,09

(continued)

Appendix (continued)

	Al14		Al15		Al17		Al21		Al22		Al25		Al26	
	I	II	I	II	I	II	I	II	I	II	I	II	I	II
Fe ₂ O ₃	7,49	14,36	12,2	15,39	11,06	9,95	14,41	12,72	11,54	11,78	13,17	12,74		
Mn ₂ O	0,08	0,15	0,34	0,28	0,16	0,1	0,44	0,32	0,17	0,22	0,12	0,21		
CaO	24,35	23,78	23,3	23,3	23,7	23,98	23,75	23,58	23,69	23,61	23,57	23,3		
H ₂ O ¹	3,69	3,7	3,64	3,65	3,7	3,74	3,52	3,52	3,75	3,78	3,75	3,73		
Sum	100,4	102,3	100,5	101,1	101,4	101,4	99,79	99,26	101,73	102,5	102,04	101,7		
Si	3,000	3,000	3,000	3,000	3,000	3,000	3,000	3,000	3,000	3,000	3,000	3,000		
Al	2,596	2,306	2,278	2,084	2,380	2,423	2,205	2,350	2,330	2,340	2,246	2,293		
Cr	0,002	0,002	0,006	0,002	0,003	0,000	0,000	0,001	0,004	0,000	0,005	0,006		
Fe ³⁺	0,454	0,731	0,744	0,945	0,667	0,597	0,916	0,810	0,694	0,702	0,793	0,771		
Mn ³⁺	0,005	0,017	0,021	0,017	0,010	0,006	0,028	0,021	0,010	0,014	0,007	0,013		
Ti	0,013	0,006	0,006	0,000	0,008	0,009	0,002	0,007	0,012	0,009	0,002	0,010		
Ca	2,103	2,060	2,023	2,036	2,035	2,048	2,150	2,138	2,027	2,004	2,020	2,009		
OH	2,000	2,000	2,000	2,000	2,000	2,000	2,000	2,000	2,000	2,000	2,000	2,000		

The proportions of cations are based on a normalization of Si to 3 cations;¹ value calculated; F, Cl are at detection limit

References

- Amaral G, Cordani U, Kawashita K* (1966) K–Ar dates of basaltic rocks from southern Brasil. *Geochim Cosmochim Acta* 30: 159–189
- Berman RG* (1988) Internally-consistent thermodynamic data for minerals in the system Na₂O–K₂O–CaO–MgO–FeO–Fe₂O₃–Al₂O₃–SiO₂–TiO₂–H₂O–CO₂. *J Petrol* 29: 445–522
- Berman RG* (1990) Mixing properties of Ca–Mg–Fe–Mn garnets. *Am Mineral* 75: 328–344
- Brandon MT, Roden-Tice MK, Garver JI* (1998) Late Cenozoic exhumation of the Cascadia accretionary wedge in the Olympic Mountains, northwest Washington State. *Geol Soc Am Bull* 110: 985–1009
- Brown TH, Berman RG, Perkins EH* (1989) Ge0-Calcul: Software package for calculation and display of pressure-temperature-composition phase diagrams using an IBM or compatible Personal Computer. *Comp Geosci* 14: 279–289
- Bruce RM, Nelson EP, Weaver SG, Lux DR* (1991) Temporal and spatial variations in the southern Patagonian batholith; constraints on magmatic arc development. *Spec Pap Geol Soc Am* 265: 1–12
- Cecioni G* (1955) Noticias preliminares sobre la existencia del Paleozoico superior en el archipiélago patagónico entre los 50 y los 52S. *Publicación N8, Instituto de Geología, Universidad de Chile* 8: 181–202
- Dale J, Holland TJB, Powell R* (2000) Hornblende-garnet-plagioclase thermobarometry: a natural assemblage calibration of the thermodynamics of hornblende. *Contrib Mineral Petrol* 140: 353–362
- Davidson J, Mpodozis C, Godoy E, Herve F, Munoz N* (1989) Lower Mesozoic accretion of high buoyancy guyots on the Gondwanaland margin: Diego Ramirez Island, southernmost South America. *Rev Geol Chile* 16: 247–251
- Douglas RG, Nestell MK* (1976) Late Paleozoic foraminifera from southern Chile. *US Geol Surv Prof Paper* 858: 47
- Forsythe RD* (1982) The late Paleozoic to early Mesozoic evolution of southern South America: a plate tectonic interpretation. *J Geol Soc Lond* 139: 671–682
- Forsythe R, Mpodozis C* (1983) Geología del basamento pre-Jurásico Superior en el Archipiélago Madre de Dios, Magallanes, Chile. *Bol Serv Nac Geol Min* N39: 63 p
- Forsythe R, Dalziel IW, Mpodozis C, Hall B, Barrientos S* (1981) Geologic studies in the outer Chilean fjords, R.V. Hero cruise 79-5. *Antarctic J United States* 15: 109–111
- Galbraith RF, Laslett GM* (1993) Statistical models for mixed fission track ages. *Nucl Tracks* 21: 459–470
- Gerya TV, Maresch WV, Willner AP, Van Reenen DD, Smit CA* (2001) Inherent gravitational instability of thickened continental crust with regionally developed low- to medium-pressure granulite facies metamorphism. *Earth Planet Sci Lett* 190: 221–235
- Graham CM, Powell R* (1984) A garnet-hornblende geothermometer and application to the Pelona Schist, southern California. *J Metamorph Geol* 2: 13–32
- Green PF, Duddy IR, Gleadow AJW, Tingate PR, Laslett GM* (1986) Thermal annealing of fission tracks in apatite 1. A qualitative description. *Chem Geol (Isotope Geosci Sect)* 9: 237–253
- Green PF, Duddy IR, Laslett GM, Hegarty KA, Gleadow AJW, Lovering JF* (1989) Thermal annealing of fission tracks in apatite. 4. Quantitative modelling techniques and extension to geological timescales. *Chem Geol* 79: 155–182
- Hervé F* (1988) Late Paleozoic subduction and accretion in Southern Chile. *Episodes* 11: 183–188
- Hervé F, Fanning M* (2004) Early Cretaceous subduction of continental crust at the Diego de Almagro archipiélago, southern Chile. *Episodes* (in press)

- Hervé F, Kawashita K, Munizaga F, Bassei M* (1982) Edades Rb–Sr de los cinturones metamórficos pareados de Chile Central. *Actas III Congr GeolChil II*: D116–D135
- Hervé F, Fanning M, Pankhurst RJ* (2003) Detrital Zircon age patterns and provenance of the metamorphic complexes of southern Chile. *J South Am Earth Sci* 16: 107–123
- Holland TJB* (1980) The reaction albite = jadeite + quartz determined experimentally in the range 600–1200 °C. *Am Mineral* 65: 129–134
- Holland TJB, Powell R* (1998a) An internally consistent thermodynamic data set for phases of petrological interest. *J Metamorph Geol* 16: 309–343
- Holland TJB, Powell R* (1998b) Mixing properties and activity-composition relationships of chlorites in the system MgO–FeO–Al₂O₃–SiO₂–H₂O. *Eur J Mineral* 10: 395–406
- Hurford AJ* (1990) Standardization of fission track dating calibration: Recommended by the Fission Track Working Group of the I.U.G.S. Subcommission on Geochronology. *Chem Geol (Isotope Geosci Sect)* 80: 171–178
- Hurford AJ, Green PF* (1983) The zeta age calibration of fission-track dating. *Isotope Geosci* 1: 285–317
- Hurford AJ, Hunziker JC, Stöckhert B* (1991) Constraints on the late thermotectonic evolution of the western Alps: evidence for episodic rapid uplift. *Tectonics* 10: 758–769
- Kato TT* (1985) Pre-Andean orogenesis in the Coast Ranges of Central Chile. *Geol Soc Am Bull* 96: 918–924
- Ketcham RA, Donelick RA, Carlson WD* (1999) Variability of apatite fission-track annealing kinetics. III. Extrapolation to geological time scales. *Am Mineral* 84: 1235–1255
- Kohn MJ, Spear FS, Dalziel IWD* (1993) Metamorphic P–T paths from Cordillera Darwin, a core complex in Tierra del Fuego, Chile. *J Petrol* 34: 519–542
- Kretz R* (1983) Symbols for rock-forming minerals. *Am Mineral* 68: 277–279
- Kukowski N, Lallemand SE, Malavieille J, Gutscher MA, Reston TJ* (2002) Mechanical decoupling and basal duplex formation observed in sandbox experiments with application to the Western Mediterranean Ridge accretionary complex. *Marine Geol* 186: 29–42
- Leake BE et al.* (1997) Nomenclature of amphiboles. Report of the subcommittee on amphiboles of International Mineralogical Association Committee on New Minerals and Mineral Names. *Eur J Mineral* 9: 623–651
- McMullin DW, Berman RG, Greenwood HJ* (1991) Calibration of the SGAM thermometer for pelitic rocks using data from equilibrium experiments and natural assemblages. *Can Mineral* 29: 889–908
- Martin MW, Kato TT, Rodriguez C, Godoy E, Duhart P, McDonough M, Campos A* (1999) Evolution of the late Paleozoic accretionary complex and overlying forearc-magmatic arc, south central Chile (38°–41° S): constraints for the tectonic setting along the south-western margin of Gondwana. *Tectonics* 18: 582–605
- Massonne H-J* (1995a) P–T evolution of metavolcanics from the southern Taunus mountains. In: *Dallmeyer RD, Franke W, Weber K* (eds) *Pre-Permian geology of Central and Eastern Europe*. Springer, Berlin Heidelberg New York Tokyo, pp 132–137
- Massonne H-J* (1995b) Experimental and petrogenetic study of UHPM. In: *Coleman RG, Wang X* (eds) *Ultrahigh pressure metamorphism*. Cambridge University Press, Cambridge, pp 33–95
- Massonne H-J* (1997) An improved thermodynamic solid solution model for natural white micas and its application to the geothermobarometry of metamorphic rocks. *Geol Surv Finland, Guide* 46 (Mineral equilibria and databases, Abstracts, p 49)
- Massonne H-J, Szpurka Z* (1997) Thermodynamic properties of white micas on the basis of high-pressure experiments in the systems K₂O–MgO–Al₂O₃–SiO₂–H₂O and K₂O–FeO–Al₂O₃–SiO₂–H₂O. *Lithos* 41: 229–250

- Massonne H-J, Hervé F, Muñoz V, Willner AP (1996) New petrological results on high-pressure, low-temperature metamorphism of the Upper Paleozoic basement of Central Chile. Ext Abstr 3rd Int Symp Andean Geodynamics, St. Malo, pp 783–785
- Olivares B, Cembrano J, Hervé F, Lopez G, Prior D (2003) Geometría y cinemática de la Zona de Cizalle Seno Arcabuz, Andes patagónicos. Chile Rev Geol Chile 30: 39–52
- Peacock SM (1996) Thermal and petrologic structure of subduction zones. In: *Behout GE, Scholl DW, Kirby SH, Platt J* (eds) Subduction – top to bottom. Am Geophys Union, Geophys Monogr 96: 119–131
- Pankhurst RJ, Rapela CW (1995) Production of Jurassic rhyolite by anatexis of the lower crust of Patagonia. Earth Planet Sci Lett 134: 23–36
- Powell R, Holland TJB (1999) Relating formulations of the thermodynamics of mineral solid solutions: activity modeling of pyroxenes, amphiboles and micas. Am Mineral 84: 1–14
- Ring U, Brandon MT (1999) Ductile deformation and mass loss in the Franciscan subduction complex: implications for exhumation processes in accretionary wedges. In: *Ring U, Brandon MT, Lister GS, Willett SD* (eds) Exhumation processes: normal faulting, ductile flow and erosion. Geol Soc Lond Spec Publ 154: 55–86
- Sambridge MS, Compston W (1994) Mixture modelling of multi-component data sets with application to ion-probe zircon ages. Earth Planet Sci Lett 128: 373–390
- Stöckhert B, Brix MR, Kleinschrodt R, Hurford AJ, Wirth R (1999) Thermochronology and microstructures of quartz – a comparison with experimental flow laws and predictions on the temperature of the brittle-plastic transition. J Struct Geol 21: 351–369
- Tagami T, Galbraith RF, Yamada R, Laslett GM (1998) Revised annealing kinetics of fission tracks in zircon and geological implications. In: *Van den Haute P, De Corte F* (eds) Advances in Fission-Track Geochronology. Kluwer, Dordrecht, pp 99–112
- Thomson SN, Hervé F (2003) Integration of detrital zircon fission-track and U–Pb SHRIMP ages to better estimate the timing of deposition, metamorphism and later reheating of metamorphic basement complexes at the ancestral Pacific Gondwana margin of southern Chile (42° S–52° S). Rev Geol Chile 29: 256–271
- Trouw RAJ, Simoes LSA, Valladares CS (1998) Metamorphic evolution of a subduction complex, South Shetland Islands, Antarctica. J Metamorph Geol 16: 475–490
- Vinograd VL (2002a) Thermodynamics of mixing and ordering in the diopside-jadeite system. I. A CVM model. Mineral Mag 66: 513–536
- Vinograd VL (2002b) Thermodynamics of mixing and ordering in the diopside-jadeite system. II. A polynomial fit to the CVM results. Mineral Mag 66: 537–545
- Weaver SG, Bruce R, Nelson EP, Brueckner HK, LeHuray AP (1990) The Patagonian batholith at 48° S latitude, Chile. Geochemical and isotopic variations. Spec Pap Geol Soc Am 241: 33–50
- Will T, Okrusch M, Schmädicke E, Chen G (1998) Phase relations in the greenschist-blueschist-amphibolite-eclogite facies in the system Na₂O–CaO–FeO–MgO–Al₂O₃–SiO₂–H₂O (NCFMASH), with application to metamorphic rocks from Samos, Greece. Contrib Mineral Petrol 132: 85–102
- Willner AP, Hervé F, Massonne H-J (1999) Comparison of the PTd-evolution of HP/LT metamorphic rocks in the South Shetland Islands and along the Coastal Cordillera of Chile. Abstr 8th Int Symp Antarct Earth Sci, Wellington, NZ, p 320
- Willner AP, Hervé F, Massonne H-J (2000) Mineral chemistry and pressure-temperature evolution of two contrasting high-pressure-low-temperature belts in the Chonos Archipelago, Southern Chile. J Petrol 41: 309–330

84 A. P. Willner et al.: Converging P-T paths of Mesozoic HP-LT metamorphic units

Willner AP, Pawlig S, Massonne H-J, Hervé F (2001) Metamorphic evolution of spessartine quartzites (coticules) in the high pressure/low temperature complex at Bahia Mansa (Coastal Cordillera of Southern Central Chile). *Can Mineral* 39: 1547–1569

Willner AP, Glodny J, Gerya TV, Godoy E, Massonne H-J (2004) A counterclockwise PT-path of high pressure-low temperature rocks from the Coastal Cordillera accretionary complex of south-central Chile: constraints for the earliest stage of subduction mass flow. *Lithos* (in press)

Authors' addresses: Prof. Dr. *A. P. Willner* (corresponding author), Institut für Geologie, Mineralogie und Geophysik, Ruhr-Universität, D-44780 Bochum, Germany; e-mail: arne.willner@ruhr-uni-bochum.de; Prof. Dr. *F. Hervé*, Departamento de Geologia, Universidad de Chile, Casilla 13518, Correo 21, Santiago, Chile; Dr. *S. N. Thomson*, Department of Geology and Geophysics, Yale University, P.O. Box 208109, New Haven, CT 06520-8109, USA; Prof. Dr. *H.-J. Massonne*, Institut für Mineralogie und Kristallchemie, Technische Universität, Azenbergstrasse 18, D-70174 Stuttgart, Germany